

Titan's surface: Search for spectral diversity and composition using the Cassini VIMS investigation

Thomas B. McCord^{a,*}, Paul Hayne^{a,b}, Jean-Philippe Combe^a, Gary B. Hansen^{a,c}, Jason W. Barnes^d, Sébastien Rodriguez^e, Stéphane Le Mouélic^f, E. Kevin H. Baines^g, Bonnie J. Buratti^g, Christophe Sotin^f, Philip Nicholson^h, Ralf Jaumannⁱ, Robert Nelson^g, and the Cassini VIMS Team

^a *The Bear Fight Center, P.O. Box 667, 22 Fiddler's Road, Winthrop, WA 98862, USA*

^b *Department of Earth and Space Science, University of California, Los Angeles, CA 90095, USA*

^c *Department of Earth and Space Science, University of Washington, Seattle, WA 98195, USA*

^d *Department of Planetary Science and LPL, University of Arizona, Tucson, AZ 85721, USA*

^e *Ctr. d'étude de Saclay, DAPNIA/Sap, bât. 709, 91191 Gif/Yvette Cedex, France*

^f *LPG de Nantes, U. de Nantes, 2 rue de la Houssinière, BP98802, 44322 Nantes Cedex 03, France*

^g *Jet Propulsion Laboratory, MS 183-501, 4800 Oak Grove Drive, Pasadena, CA 91109, USA*

^h *Cornell University, Department of Astronomy, Space Science Bldg., Ithaca, NY 14853, USA*

ⁱ *DLR, Institute of Planetary Research, Rutherfordstrasse 2, 12489 Berlin, Germany*

Received 10 May 2007; revised 11 August 2007

Available online 13 October 2007

Abstract

The surface composition of Titan is of great importance for understanding both the internal evolution of Titan and its atmosphere. The Visual and Infrared Mapping Spectrometer (VIMS) investigation on Cassini is observing Titan from 0.35 to 5.11 μm with spatial resolution down to a few kilometers during each flyby of the spacecraft as it orbits Saturn. Our search for spectral diversity using seven methane transmission windows in the near infrared suggests that spectrally distinct units exist on the surface of Titan and that most of the surface can be modeled using only a few distinct spectral units: water frost, CO₂ frost, atmospheric scattering, and an unknown material bright at 2 μm . A dark, spectrally neutral material is also implied. Use of an atmospheric scattering component with spectral mixing analysis may provide a method for partially removing atmospheric effects. In some locations, atmospheric scattering accounts for the majority of the signal. There are also small regions with unusual spectra that may be due to low signal and high noise and/or may be exotic materials of interest. Further, we searched within the methane windows for spectral features associated with Titan's surface. Only the 5- μm and, to a lesser extent, the 2- μm window provide a reasonable opportunity for this, as the shorter-wavelength windows are too narrow and the 2.8- μm window is cluttered with an unknown atmospheric constituent. We find evidence for only one spectral feature: near 4.92 μm for the 5- μm bright Tui Regio region. CO₂ frost with grains smaller than about 10 μm is the best candidate we have found so far to explain this absorption as well as the feature's spectral contrast between the 2.7- and the 2.8- μm atmosphere subwindows. This suggested CO₂ identification is supported by the presence of an endmember in the spectral mixture analysis that is consistent with CO₂ frost with large grain sizes. We find no other absorption features that are statistically significant, including those reported earlier by others. These results are consistent with but greatly extend our early analysis that treated only the T_a data set [McCord, T.B., et al., 2006a. *Planet. Space Sci.* 54, 1524–1539]. In the spectral feature search process, we explored in detail the noise characteristics of the VIMS data within the 5- μm window, which has generally very low signal (4–20 DN), due to the measurement conditions and low illumination levels. We find noise of nearly Gaussian statistics except for some erratic darks and noise spikes, and the data set seems generally well behaved. We present examples of our attempt to improve on the standard VIMS pipeline data calibration.

© 2007 Elsevier Inc. All rights reserved.

* Corresponding author.

E-mail address: mccordtb@aol.com (T.B. McCord).

Keywords: Saturn, satellites; Satellites, surfaces; Spectroscopy

1. Introduction

The composition of Titan's surface was recently investigated by reflectance spectrophotometry using some of the earliest measurements of Titan from the Cassini mission Visual and Infrared Mapping Spectrometer (VIMS) (McCord et al., 2006a, 2006b). A review of earlier work on the subject is included in this previous publication. That history consists mostly of several groundbased telescope spectroscopic studies of Titan, culminating in the Griffith et al. (2003) study and showing that the spectra are consistent with the presence of "dirty" water ice such as is found on Ganymede. The VIMS data are the first with significant (<1 to ~ 10 km) spatial resolution on Titan. The McCord et al. study reported that spectral properties of dark areas are consistent with water ice containing a neutral darkening material, but the bright regions are more varied and are not consistent with any material considered. Organic materials, especially tholins, have been widely suggested to exist on Titan (e.g., Cruikshank et al., 1991; Griffith et al., 2003; Bernard et al., 2006), but no spectral evidence of them was found.

We have extended this study using many more recent VIMS data for Titan and we report here on our findings through Titan flyby T23. We use two different approaches: (1) Spectral Mixture Analysis (SMA) using I/F values averaged over several spectral channels within seven atmospheric spectral windows to determine the number and type of basic spectral units present, and (2) a search for spectral absorption features at VIMS full spectral resolution within the methane windows.

The difficulty in studying Titan's surface from space is of course its thick, hazy and absorbing atmosphere. The atmosphere is approximately 1.5 bar pressure at the surface and contains approximately 5% methane, which absorbs heavily in the VIMS spectral range. Scattering particles also are present, with their effect increasing toward shorter wavelengths. These effects vary in space and time. Thus, the surface is visible only within a few narrow, hazy spectral windows between strong methane absorptions. Radiative transfer modeling of the atmosphere is a useful technique for reducing the haze effects within the methane windows and for extending the useful edges of the windows, but this approach is difficult because of the strong effects of the scattering and absorption and their variability with altitude and with location (cf. Griffith et al., 2003). The Huygens probe measurements (Tomasko et al., 2005; Flasar et al., 2005; Fulchignoni et al., 2005) greatly increased our knowledge of these atmospheric effects, but only at one location and time. Thus, atmospheric modeling remains in an early stage. For this study, we do not attempt radiative transfer modeling to remove atmospheric effects, although we provide a potential alternative method for estimating the scattering contributions within the methane windows.

2. Observations

We treat VIMS data sets ranging from flybys T03 to T23, among the larger set of data available. The earlier McCord et al. study treated only the T_a data set. These later data sets cover a sufficient variety of regions and conditions to provide a much better basis than the earlier study.

Although Cassini encounters Titan on almost every orbit of Saturn, there is considerable competition for spacecraft data storage and downlink capacity during these flybys, and the encounters are of short duration, so that the VIMS data collected is limited. Further, celestial mechanics constrains the variety of viewing geometries possible, limiting the Titan regions covered. In addition, because of the short duration of the encounters, limited observation time available for VIMS, low light levels, and the competing desire for maximum areal coverage, the signal-to-noise ratio of many of the data sets is low, especially at $5\ \mu\text{m}$ (Table 1).

The data sets are first received by the VIMS investigation as digital numbers (DN) for each spectral channel and pixel of spatial resolution. These are as provided by the 12-bit analog-to-digital converter in the instrument (Brown et al., 2004). These DN values, after (lossless) data compression on-board and decompression on the ground, are then treated by the calibration tables developed for the instrument, using ground and flight measurements (Brown et al., 2004; McCord et al., 2004), to calculate radiance, and then divided by the incident solar radiation to calculate I/F , or radiance factor (e.g., Hapke, 1993). We use these I/F values as provided by the VIMS "pipeline" or standard processing system, except where noted. This of course is I/F for the scene at the top of the atmosphere and does not yield directly the optical properties of the surface material, due to atmospheric contributions. In most cases we use VIMS data before spatial resampling for mosaicking or reprojecting onto a map base, and we maintain knowledge of the original pixel DN values to estimate signal and noise statistics.

3. Spectral units identity and diversity

3.1. Calibration and spectral windowing

We first searched for evidence of regions of distinct spectral properties. Evidence was reported for the existence of spectral units on the surface and two main compositional units were identified, associated with bright areas and dark areas, plus several areas of "unusual" spectral behavior (McCord et al., 2006a, 2006b; Rodriguez et al., 2006; Barnes et al., 2007), such as evidenced in spectral ratio images. These unusual areas include the $5\text{-}\mu\text{m}$ -bright regions such as that now called Tui Regio (Barnes et al., 2005, 2006, 2007; McCord et al., 2006a, 2006b). In McCord et al. (2006a, 2006b) spectra were extracted for these units, an attempt was made to remove the atmosphere effects using radiative transfer models to obtain surface I/F , and these

Table 1

The mosaic data sets used in the spectral feature search are described here. They were prepared by the German Space Center DLR (Jaumann et al., 2006)

Mosaic	Sequence #	Cube name	Date	Integration (ms)	Average and DN range 5 μm
TI019_HDAC001	S17	CM_1514302573	Dec-26-05	80	5.3, 1–24
		CM_1514302990	Dec-26-05	320	21.9, 7–65
		CM_1514304423	Dec-26-05	320	19.8, 7–57
		CM_1514305926	Dec-26-05	640	41.9, 11–83
		CM_1514309549	Dec-26-05	160	9.8, 2 ^a
		CM_1514310267	Dec-26-05	160	9.1, 3–21
		CM_1514313117	Dec-26-05	160	8.8, 3–23
		CM_1514313835	Dec-26-05	160	10.2, 3–24
		CM_1514315553	Dec-26-05	80	5.8, 1–31
		CM_1514315913	Dec-26-05	80	5.5, 1–23
		CM_1514316735	Dec-26-05	80	4.6, 2–47
		CM_1514317135	Dec-26-05	80	5.0, 2–16
		TI003_GLOBMAP001	S08	CM_1487118608	Feb-15-05
CM_1487118864	Feb-15-05			640	40.2, 23–57
CM_1487119120	Feb-15-05			640	29.0, 21–44
CM_1487119376	Feb-15-05			640	39.7, 25–64
CM_1487119632	Feb-15-05			640	61.4, 43–73
CM_1487119937	Feb-15-05			640	68.6, 55–87
CM_1487120447	Feb-15-05			640	33.7, 24–53
CM_1487120702	Feb-15-05			640	52.3, 32–253
CM_1487120957	Feb-15-05			640	54.4, 41–64
CM_1487121258	Feb-15-05			640	51.4, 41–66
CM_1487121516	Feb-15-05			640	40.0, 29–52
CM_1487121774	Feb-15-05			640	35.0, 23–63
CM_1487122032	Feb-15-05			640	62.8, 31–81
CM_1487122290	Feb-15-05			640	72.9, 56–87
CM_1487122597	Feb-15-05			640	75.8, 55–137
CM_1487122854	Feb-15-05			640	68.9, 56–114
CM_1487123111	Feb-15-05			640	54.0, 28–71
CM_1487123368	Feb-15-05			640	47.9, 34–63
CM_1487123625	Feb-15-05			640	54.2, 48–66
CM_1487123925	Feb-15-05			640	50.0, 33–62
CM_1487124186	Feb-15-05	640	62.4, 50–76		
CM_1487124708	Feb-15-05	640	62.5, 52–85		
CM_1487124969	Feb-15-05	640	72.7, 48–146		

^a Saturation of the detector.

surface spectra were compared with laboratory spectra for candidate materials. In the present study, we treated many more data sets, used an empirical model to remove atmosphere effects, searched for more spectral variety and attempted to map the spectral units by taking into account potential spectral mixtures. In general, we are seeking a better measure of the spectral diversity and its relationship to surface albedo and morphologic features.

The method presented in this section is focused on the analysis of the overall spectral shapes present in VIMS data. An example spectrum is shown in Fig. 1, which is obtained by averaging I/F values for 1.094 pixels in data set CM_1525118253 from sequence S20. The spectral range (0.8–5.1 μm) corresponds to the VIMS IR channel. The peaks in the spectrum are regions of least methane absorption, between the strong methane bands, and where the surface I/F contribution is greatest (marked by gray tone vertical bars in Fig. 1). Included in this spectrum is the contribution of atmospheric particle scattering, which is strongest at shorter wavelengths and decreases almost to zero contribution at the 5- μm window. Images were calculated for each window by averaging the several spectral

channels within the window to increase the signal-to-noise ratio (SNR). Two-to-ten spectral channels are averaged within each window (Table 2), the widest being the 5- μm window.

3.2. Data selection and registration

The purpose of our analysis is to identify the main spectral units at the surface of Titan. This requires data from the largest possible observed area, thus the highest possible number of images. However, because the VIMS data set has been acquired under extremely diverse illumination and observation geometries and instrumental modes, all the images are not useful or comparable and should not be processed in the same way. When a surface is poorly illuminated due to high solar incidence angle, the signal to noise ratio is low, which enhances instrumental artifacts. In addition, both high incidence and emergence angles may enhance atmospheric-related effects. For these two reasons, the pixels observed at incidence angle larger than 70 degrees (about 1/3 of the illumination flux at the sub-solar point of the surface) and emission angle larger than 45 degrees are masked. Masking is also applied to avoid erroneous data (i.e.,

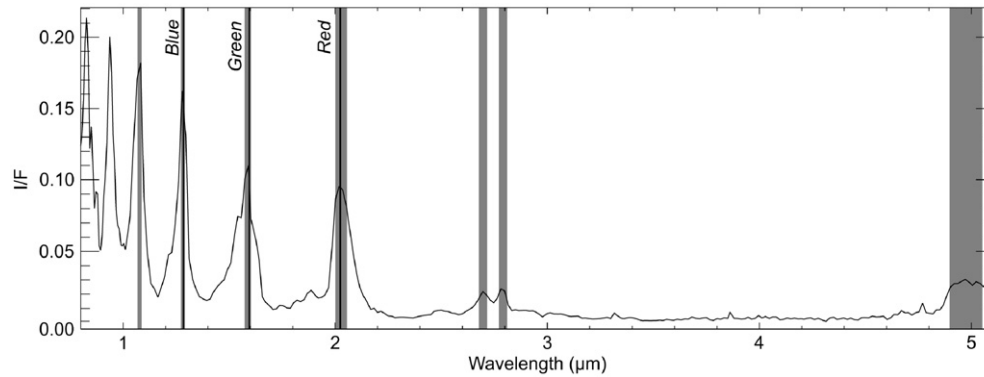


Fig. 1. Example spectrum for Titan from the VIMS infrared channels. The peaks in the spectrum correspond to the spectral regions between methane absorptions where the surface is reachable. The seven longest wavelength windows are marked with vertical bands. The 2.8- μm window is composed of two subwindows maybe due to a yet-unidentified absorption in the center (McCord et al., 2006a, 2006b).

Table 2

The spectral channels within each methane window that were averaged to produce the images analyzed for spectral diversity are given here

Minimum wavelength (μm)	Maximum wavelength (μm)	Number of averaged channels
1.244920	1.278130	3
1.524210	1.590180	5
1.968710	2.067570	7
2.661460	2.696200	3
2.763050	2.781180	2
4.902650	5.074020	10

I/F less than 0 or greater than 1 for a given channel). When this occurs, the whole spectrum is masked.

The data registration is checked by displaying the data on a cylindrical projection map at 10 pixels per degree, where the highest spatial resolution data are displayed in the foreground. Several steps are necessary to build this mosaic, because of errors in the spatial registration. These result from uncertainties in the latitudes and longitudes provided by the pipeline calibration. Mis-registration errors may be up to 8 degrees between images from different sequences, and up to 3 degrees between images within the same sequence. To correct for these errors, we first build a mosaic for each sequence of observation. These mosaics are compared to a global map of the Imaging Science Subsystem (ISS) images of Titan (available at <http://ciclops.org/maps/maps.php>) taken as a reference (gray background in Fig. 2). This first comparison may enhance different errors within the same sequence. If these occur, each sequence may be split in several parts and compared to the reference, and finally corrected. A simple shift in latitude and longitude is obvious in most of the cases, while rotation and dilatation occur less often. When shifts in the two spatial dimensions are not sufficient, the data are discarded because a correction in the navigation system would be more suitable in such cases.

Finally, data homogeneity is reviewed visually by comparing the images for the seven spectral windows within a mosaic, and then between several mosaics. One or several image cubes of a mosaic were removed when a high contrast occurs between the edge of an image in the foreground and the image in the

background. This is probably due to effects that are highly sensitive to the geometry of illumination and observation, or local changes in time in the atmosphere. After data selection, the final mosaic considered in this section (colored foreground in Fig. 2) covers areas around the Shangri-La and Fensal regions of Titan's anti- and sub-saturnian hemispheres, respectively. The data displayed have been divided by the cosine of the incidence angle in order to scale the illumination of the surface to a normal incidence, and to make the data more comparable. A large part of the surface of Titan has been masked because of insufficient illumination and therefore very low SNR due to being near a terminator or limb, as discussed above.

3.3. Spectral Mixture Analysis method

This approach is focused on the analysis of the global shape of spectra and the combination of spectra to explain this shape. The Spectral Mixture Analysis (SMA) approach is suited to the deconvolution of spectra, given a set of spectral components. The technique we use here is based on linear combinations of spectra that describe macroscopic mixtures (Adams and McCord, 1971; Nash and Conel, 1974; Singer and McCord, 1979). While non-linear spectrum mixtures are expected to occur in VIMS data, the purpose of the SMA approach is to separate mixtures of constituents and map their relative variations (Adams and Gillespie, 2006) rather than calculating their absolute proportions. We used here the same equation of inversion as Ramsey and Christensen (1998), based on the root-mean square (RMS) minimization. Each spectrum (pixel) of the image is processed independently. The major drawback of this method is that it may provide negative coefficients of unmixing. This means that the opposite shape of some spectra is used in the model. Such results have no physical meaning. To avoid negative coefficients, Ramsey and Christensen (1998) and Combe et al. (2006) developed iterative methods. We used here an algorithm that calculates all the possible combinations of spectra. For each spectrum in an image, the closest model (minimum chi-square residual) is selected.

The algorithm is constrained so that the number of components used to model a spectrum must be less than the number of spectra in the input library. No constraint is applied to the value

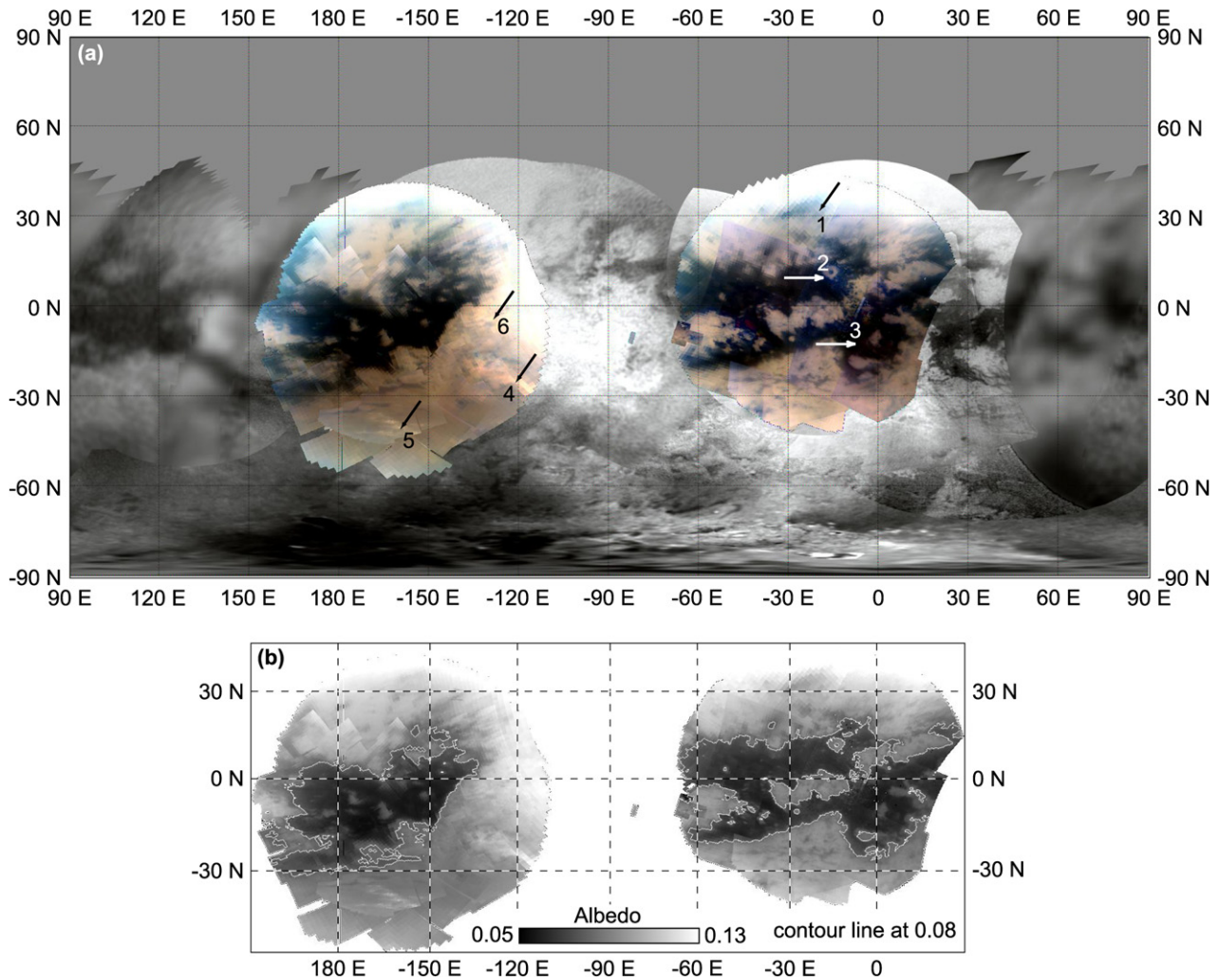


Fig. 2. (a) A false-color georeferenced mosaic of *I/F* VIMS Titan data sets that were analyzed for spectral diversity are shown. The three wavelength bands of the Titan VIMS spectrum used and the display color scheme is defined in Fig. 1: red = 1.28 μm; green = 1.59 μm; blue = 2.03 μm. Three main units appear: bright, dark and blue materials. The numbers from 1 to 6 refer to the location of the spectral endmembers in Fig. 3a. The foreground is a mosaic of observations by the Imaging Science Subsystem (ISS); credit: NASA/JPL/Space Science Institute. (b) Albedo image calculated by averaging the seven bands selected for this analysis, with a superimposed contour line at 0.08 to help localizing positions.

of the unmixing coefficients because spectral mixtures follow processes that are not always linear. As a consequence, the sum of all the coefficients is not necessarily one.

3.4. The major spectral components

To some extent, spectral diversity can be discerned in a simple three-color composite of images. Using each of three methane windows (Fig. 2) and the color scheme red = 2.03 μm, green = 1.59 μm, blue = 1.28 μm, three main spectral units appear: bright, dark and blue materials. The bright and dark units are as seen in single-spectral-channel gray-scale images at most wavelengths and discussed by McCord et al. (2006a, 2006b). The blue unit appears to occur in association with both of the other two units, but more so with the dark unit. The circular feature Sinlap at -15 E, 5 N, has been identified as an impact crater by Stofan et al. (2006), and is flanked by blue material extending in the southeastern direction.

Improvements to the above qualitative analysis are made by using all spectral windows and quantifying endmember selection. The first step is to choose the spectral endmembers. They can be extracted from VIMS data (image endmembers), but spectra of pure materials are not expected in VIMS data. When spectral endmembers are not pure materials, SMA results are difficult to interpret. Because of this, we prefer using reference spectra of pure materials from laboratory measurements. We used the automatic extraction of image spectral endmembers in order to select spectral endmembers from laboratory measurements, with the help of previous studies to know which materials are expected on Titan.

3.4.1. Searching for image spectral endmembers

In this study, the Pixel Purity Index (PPI) tool of the Environment for Visualizing Images (ENVI) software (Boardman et al., 1995) is used to help determine the number and type of the purest spectral endmembers present in a data set. This

tool searches the entire data set for the most extreme spectral shapes. It is based on the statistical principal components resulting from a Minimum Noise Fraction (MNF) transform. The PPI technique is based on random rotations around all the axes of the principal components, and thus, the calculation is more efficient when performed on non-projected and resampled data. In addition, projecting the mosaic may result in pixel aggregation or pixel superimposition by other data, meaning a loss of spectral diversity with respect to the original data. Performing the PPI on a set of images requires first building a mosaic of juxtaposed non-projected data. The PPI provides $N + 1$ spectra, with N the number of wavelength channels. Here, these correspond to the seven spectral windows shown in Fig. 1 and Table 2. Thus, eight spectral endmembers are obtained via PPI.

The spectral endmembers with the most extreme spectral shapes are not necessarily spectral components. In practice, the PPI tool selects possible spectral components, but some of these may not be appropriate inputs for the SMA. For example, PPI may generate endmembers that are qualitatively too similar to others, and these have to be removed. However, the purpose at this stage is simply to provide a set of spectra that can be compared to spectra of actual materials. These image endmembers are not used as input for the SMA. Fig. 3 shows our selection of the most extreme spectral endmembers—we attempted to associate these spectral shapes with known materials, taking into account scattering by the atmosphere.

3.4.2. Atmospheric scattering model

Atmospheric scattering results in additive contributions in remote sensing spectra (van de Hulst, 1981; Gaddis et al., 1996; Bohren and Huffman, 1998; Sobolev, 1975; Rodriguez et al., 2006). The regimes of atmospheric scattering depend on particle size with respect to the wavelength of incident radiation. Non-absorbing particles that are large (>10 times) or small (<0.1 times) with respect to the wavelength scatter radiation in ways described by Mie (1908) and Rayleigh (1971) models, respectively. Particles roughly equivalent in size to the wavelength are likely absorbers. To calculate the amount of backscattered light in a spectrum, physical models use optical constants of aerosol materials and particle sizes as inputs (e.g., Sobolev, 1975). For example, Rodriguez et al. (2006) assume a single layer of tholins with an average particle radius of $0.18 \mu\text{m}$. In the present study, we derive information about atmospheric scattering from the SMA, assuming it is an additive contribution that follows a decreasing monotonic function of the wavelength. Atmospheric backscattering contributions described by Rodriguez et al. (2006) may be fitted by a polynomial function P of the form:

$$P(\lambda) = a + b\lambda^{-1} + c\lambda^{-2} + d\lambda^{-3} + e\lambda^{-4}, \quad (1)$$

where λ is the wavelength, a , b , c , d and e are scalars. The SMA provides these scalars for each pixel independently, in the same way as the unmixing coefficients of spectral endmembers. This means all five parameters are set to be positive, which reduces the degrees of freedom. This function corresponds to the part of the spectra that cannot be explained by the spectral components of the surface. It is always a monotonic function of wavelength,

which varies smoothly from pixel to pixel, and we assume it is mainly due to atmospheric scattering.

We did not use a template spectrum from limb observations, where the signal is almost entirely produced by atmospheric scattering. The reason is that variations in atmospheric scattering may occur between different parts of the disk, and this cannot be taken into account using a single image endmember.

3.4.3. Spectra of surface materials

Probable components at the surface of Titan have been derived first from Earth-based telescopic spectroscopy. H_2O ice has been detected first by Griffith et al. (2003) and Lellouch (2006). Other materials have been suggested, such as CO_2 ice (Griffith et al., 2003; Coustenis et al., 2006), bitumens Lellouch (2006), and CH_4 ice (Coustenis et al., 2006). Previous studies using VIMS spectra from the Huygens landing site and from the DISR/Huygens spectrometer concluded that probable components at the surface, in that region, may be H_2O ice (Tomasko et al., 2005; Rodriguez et al., 2006), CH_4 ice, tholins (Tomasko et al., 2005), and CO_2 ice (Rodriguez et al., 2006). The Tui Regio bright spot was also found to have $5\text{-}\mu\text{m}$ reflectance compatible with CO_2 (Barnes et al., 2005). However, representative surface spectra in Fig. 3 are not obviously related to a composition of H_2O ice, CH_4 ice (Grundy et al., 2002) and tholins (Cruikshank et al., 1991 in Griffith et al., 2003; Bernard et al., 2006).

Spectrum 1 shows some similarities to CO_2 ice spectra (Fig. 4a) of some grain sizes, in particular the overall V shape of both spectra. Bright material spectra (numbers 4, 5 and 6), also share features with small grain size CO_2 ice: they have the same asymmetry in the double window at 2.71 and $2.78 \mu\text{m}$, with lower values (higher absorption) at the shorter wavelength. The SMA results in Fig. 4b demonstrate that Spectrum 1 can be modeled accurately (chi-square $\sim 1\%$) by a linear mixture of laboratory CO_2 ice spectra (Hansen, 1997) and the polynomial atmospheric scattering model. In what follows, we use the three CO_2 ice spectra in Fig. 4a as inputs to the SMA, rather than Spectrum 1. In the results, image fractions of the three CO_2 components are summed to provide a single CO_2 ice end-member map, because SMA lacks the precision to evaluate the particle size.

The presence of water ice in dark regions has been suggested by Tomasko et al. (2005) using data from the Descent Imager/Spectral Radiometer (DISR) instrument of the Huygens probe, as well as by Rodriguez et al. (2006) and by McCord et al. (2006a, 2006b) based on VIMS data and by Griffith et al. (2003) from groundbased telescope data. In what follows, we used modeled spectra of H_2O ice at 110 K provided by Hansen and McCord (2004). These are calculated by scattering and albedo computation (Wiscombe and Warren, 1980) from optical constants by Grundy and Schmitt (1998). Water ice spectra at different grain sizes show strong variations in spectral shape, even when resampled to the seven usable VIMS bands (Fig. 5). Only the $100 \mu\text{m}$ grain size H_2O ice spectrum was included in the model, because it has high values at 1.07 and $1.28 \mu\text{m}$, similar to the spectra of VIMS dark blue units. Spectra of fine grain size H_2O samples have

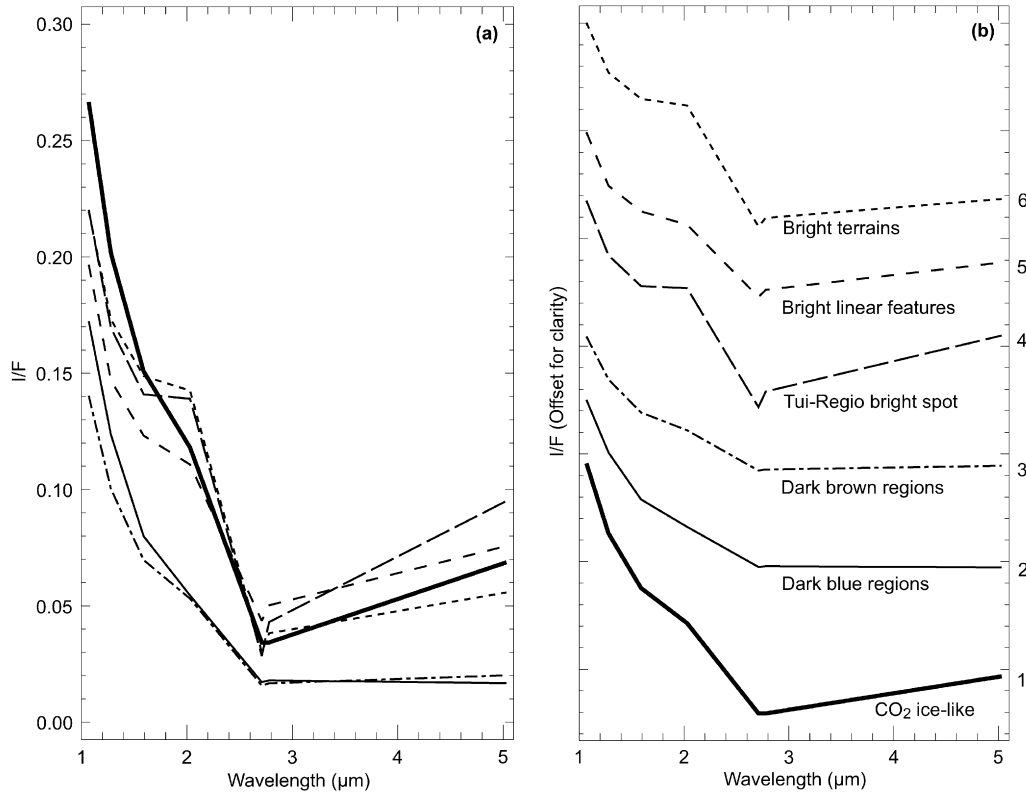


Fig. 3. (a) A selection of the most extreme spectral shapes (endmembers) found by the Pixel Purity Index (PPI) tool of the Environment for Visualizing Images (ENVI) software are shown. The location where these spectral endmembers come from are identified with numbers and arrows on the color composite mapped in Fig. 2. (b) The same spectra offset along the vertical axis for clarity.

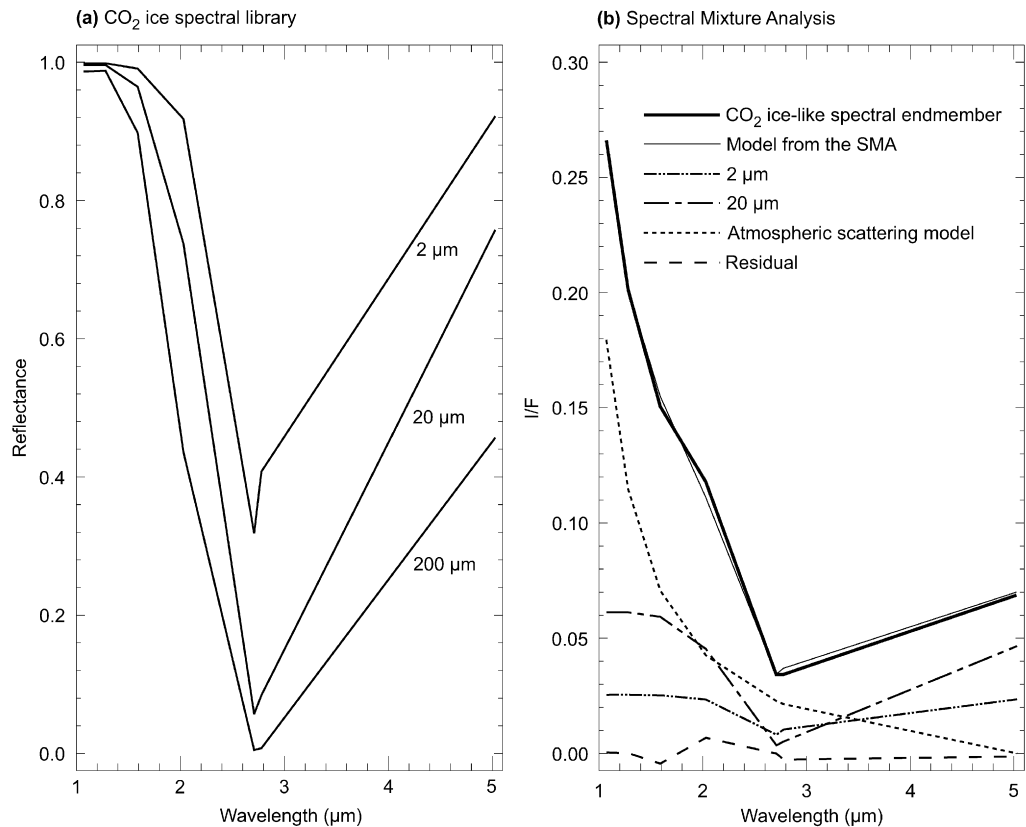


Fig. 4. Spectral Mixture Analysis applied on the CO₂ ice-like endmember. Three CO₂ ice spectra (a) and the polynomial atmospheric scattering model are combined linearly to provide an accurate (chi-square ~1%) fit (b).

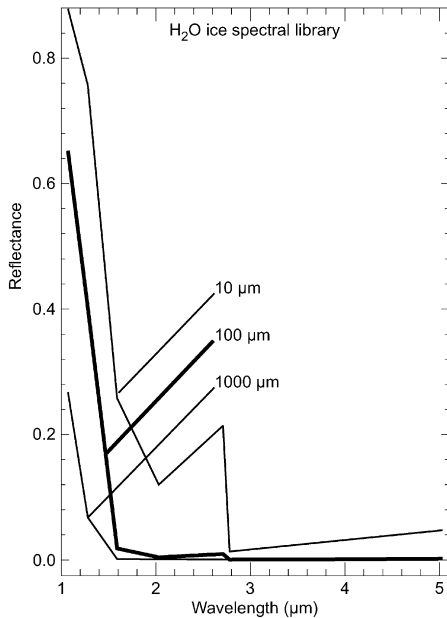


Fig. 5. H₂O ice spectra with various grain sizes show different shapes, even when sampled in the seven spectral atmospheric windows of Titan. The 10 μm grain size sample shows spectral features that are never encountered in any of VIMS measurements. The spectrum of the 100 μm grain size sample has low I/F values at all the wavelengths, except at the two shortest bands, and is a potential component for the dark blue regions. H₂O ice with grain size of 1000 μm has a spectral shape very similar to some scattering by fine aerosol particles or by gases, and thus. The 100 μm grain size spectrum has been selected to perform the SMA.

sharp spectral features, in particular a local minimum at 2 μm and sharp negative slope in the double window between 2.71 and 2.78 μm . These features are not observed in any of the VIMS measurements, and thus the spectrum was not included in the SMA. The 1000 μm grain size H₂O ice spectrum shows an increase towards shorter wavelengths, very similar to the atmospheric scattering model. Because of this similarity, it was not included in the input reference spectra library for the SMA.

The positive slope in the double window at 2.71 and 2.78 μm observed in Titan spectra is compatible with fine-grained CO₂ ice, but not with fine-grained H₂O ice. Coarse-grained H₂O ice is spectrally neutral in this wavelength range. However, laboratory measurements by Bernstein et al. (2005) show that this slope may be preserved in intimate mixtures of CO₂ ice and H₂O ice. According to Coustenis et al. (2006), this increase in albedo in ISO data is also an argument for the possibility of CO₂. Further, the CO₂ absorptions at 2.69 and 2.78 μm are shifted towards longer wavelengths in these mixtures, closer to the centers of Titan's atmospheric windows. Thus, the behavior of the double window may be explained by the presence of CO₂ ice mixtures on Titan's surface.

For comparison purpose, Fig. 6 shows the same VIMS end-member spectra than Fig. 3, and laboratory spectra for CH₄ ice, CO₂ ice (the same as Fig. 4a) and H₂O ice (the same as Fig. 5).

Though the remaining spectral endmembers share some common features, they cannot be modeled completely by CO₂ ice, H₂O ice, and the atmospheric component. Thus, these spec-

tra most likely represent different surface compositions, and we named them for their respective geographical origins: the dark blue regions (Soderblom et al., 2005, 2007), the dark brown region (Soderblom et al., 2005, 2007), the Tui Regio bright spot (Barnes et al., 2005, 2006, 2007; McCord et al., 2006a, 2006b), the bright linear features and the bright terrains. In addition, several of the spectral endmembers in Fig. 3 have a discontinuity in slope at 2 μm that may be due to a shared component. In order to isolate this component, we performed the SMA using only the CO₂ ice spectra, the H₂O spectrum, and the atmospheric scattering model, and then calculated statistics for the residual image.

When an insufficient number of spectral endmembers is used in the SMA, the spectral shape of the residual is expected to contain some information about the missing spectral components. The inversion of the linear combination equation provides a unique solution when the number of unknown variables (spectral endmembers) is lower than or equal to the number of equations (seven, the same as the number of wavelength channels). Thus, the program is set to use either a maximum of three spectral components with a maximum of four coefficients in the atmospheric scattering model, or a maximum of two spectral components with a maximum of five coefficients in the atmospheric model. The residual spectrum and the chi-square statistic are calculated for each pixel.

The chi-square image is displayed in Fig. 7a. Figs. 7b to 7h show the data clouds of the residual for each wavelength versus the chi-square value. The linear shape and the oblique orientation of the clouds at each wavelength indicate the residual is correlated to the chi-square value when the slope is positive and anti-correlated when the slope is negative. This linearity means that these residuals are not random, despite the 5 degrees of freedom of the polynomial atmospheric scattering model. It also implies that only one more spectral component is necessary to accurately model the VIMS data. The most representative spectral shape of the residual is calculated by linear regressions (see the equations on the graphs) at each wavelength for the data points that correspond to chi-square values greater than 5%. This value is an estimation of the data uncertainties (gray ranges on the graphs). It corresponds also to the most linear part of the data clouds.

The typical spectral shape associated with the residuals is displayed in Fig. 7i (thin solid line spectrum). This spectrum has negative values, and thus must not be used as a spectral end-member in the SMA. The most remarkable feature is the high I/F value at 2 μm . The shape in the double window at 2.7 μm is similar to the fine-grained CO₂ ice spectra. Among the possible materials that may be present on Titan (CH₄, C₂H₆, H₂O, CO₂ ices and tholins), only the fine-grained CO₂ ice spectrum has a spectral shape similar to the residual spectrum. Assuming this shape is due to CO₂ ice only, we infer the SMA is deficient in that component. On the other hand, the negative value at 5 μm indicates an excess of the large-grained CO₂ ice spectrum, because this is the only endmember used in the SMA that has large values at 5 μm . High values at 2 μm and at shorter wavelengths in the residual spectrum cannot be explained by the CO₂ ice and atmospheric scattering spectral endmembers.

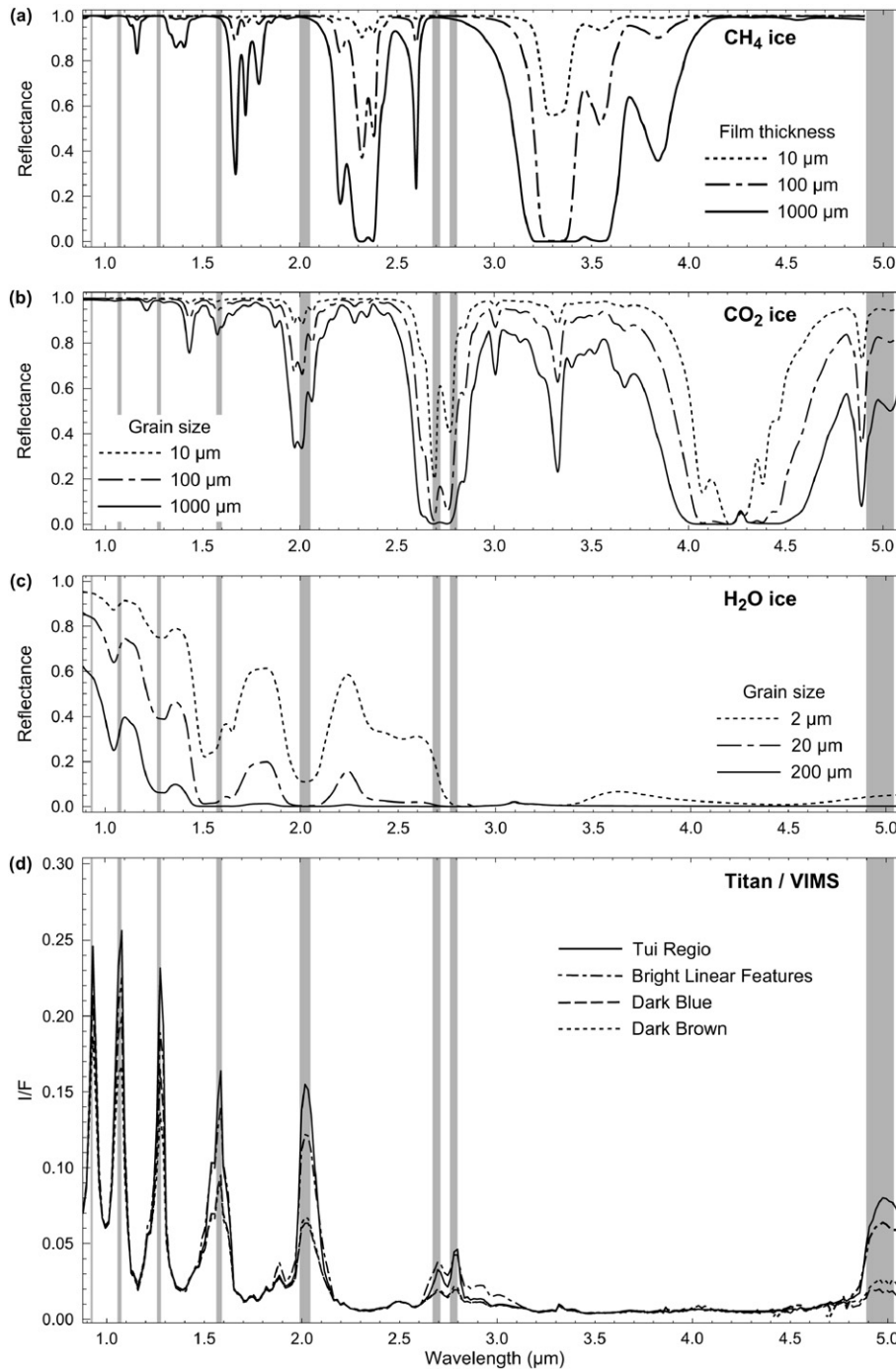


Fig. 6. Spectra at full VIMS resolution (a)–(c). Laboratory spectra for each of the candidate materials. (a) CH_4 data from Grundy et al. (2002). (b) CO_2 data is taken from Hansen (2005). (c) H_2O ice at 110 K provided by Gary Hansen. (d) VIMS spectra for each of the major surface endmembers.

Thus, the characteristic spectral shape of the unknown component is given by the 1–2 μm wavelength range. The residual spectral shape may be iteratively corrected to calculate a plausible spectrum for the unknown component. This is obtained by adjusting the proportions of the CO_2 ice spectra and the polynomial atmospheric scattering model in order to reach positive values at all the wavelengths and to minimize all the spectral features in the range 2.7–5 μm . The result is shown as the bold line in Fig. 7i. This spectrum still has the main spectral features of the residual spectrum and meets all the mathematical

requirements to be included as a regular endmember input to the SMA.

3.4.4. Spectra of actual materials used to fit image spectral endmembers

A further test of the SMA consists of using the three CO_2 ice spectra, the 100- μm grain size H_2O spectrum, the calculated bright component at 2 μm and the polynomial atmospheric scattering model to fit the six spectral endmembers in Fig. 3. The SMA is performed on the windowed 7-channel spectra.

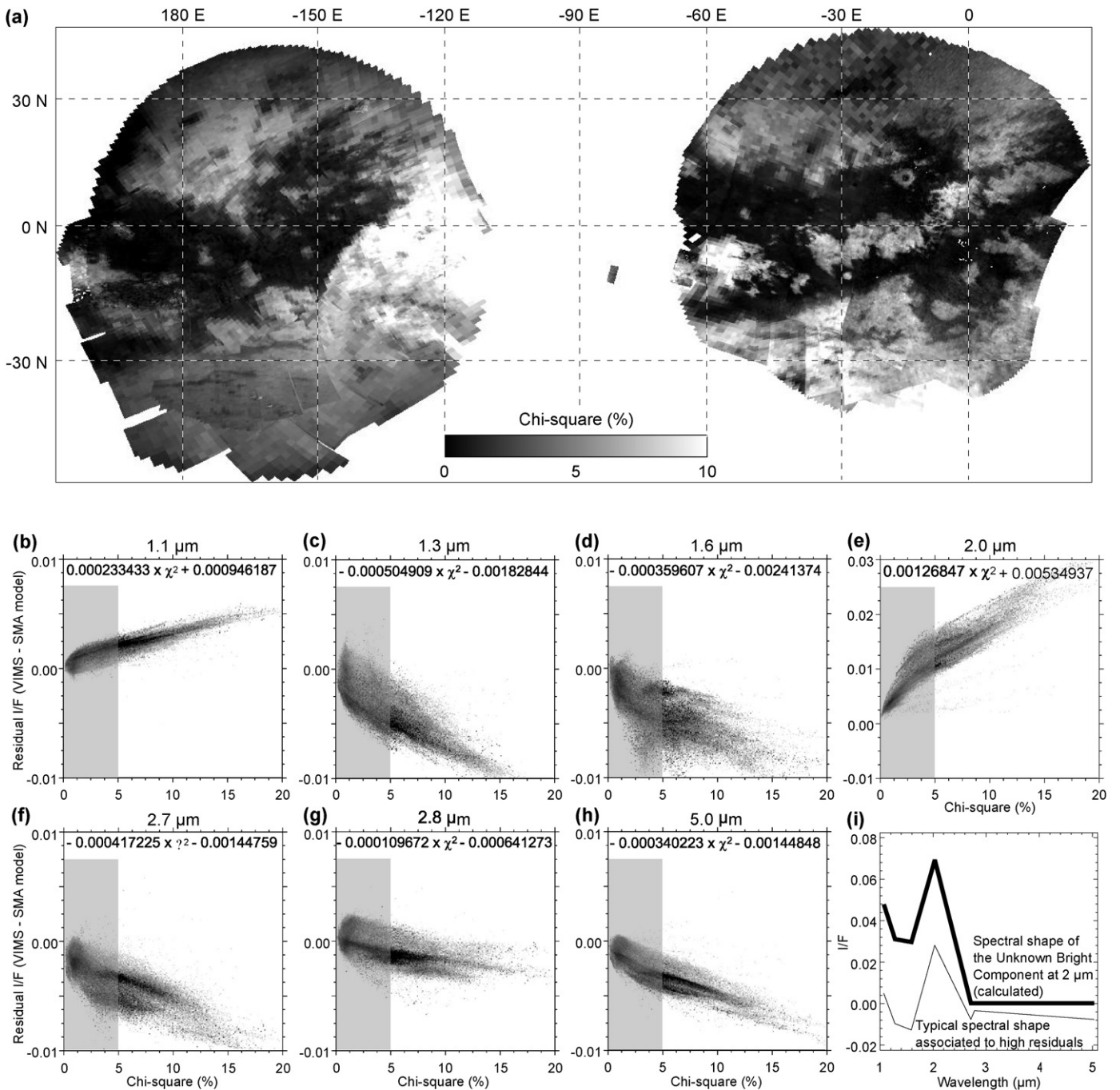


Fig. 7. Statistical analysis of the SMA residuals using CO_2 ice spectra, the H_2O spectrum and an atmospheric scattering model. (a) Image of the chi-square residual. (b-h) Residual differences between VIMS spectra and the SMA model at the seven atmospheric windows. (i) Spectral shape of the residual and spectral shape proposed for an unidentified bright component at $2 \mu\text{m}$.

The linear spectral unmixing algorithm is constrained to use no more than three spectral endmembers at a time for a total of no more than seven simultaneous parameters. This means a maximum of four atmospheric parameters may be used when three spectral endmembers are present in the model. In this case, the constant term of the polynomial is set to zero. The results are shown in Fig. 8. All the models fit the spectra under the 1% chi-square limit. The CO_2 ice spectra, the calculated bright component at $2 \mu\text{m}$ and the atmospheric scattering polynomial are necessary for all of them. For the dark blue region spec-

trum (Fig. 8a), the H_2O ice spectrum has a small but significant contribution, while the atmospheric scattering component has the highest spectral contribution. The relative proportions of the other materials in decreasing order are CO_2 ice and the calculated bright component at $2 \mu\text{m}$. Low I/F values are consistent with other surface components of dark blue regions having a low albedo in all atmospheric windows (i.e., a flat spectrum), which has been reported previously as consistent with dirty water ice (Griffith et al., 2003; McCord et al., 2006a, 2006b; Soderblom et al., 2007). The spectrum from the dark brown re-

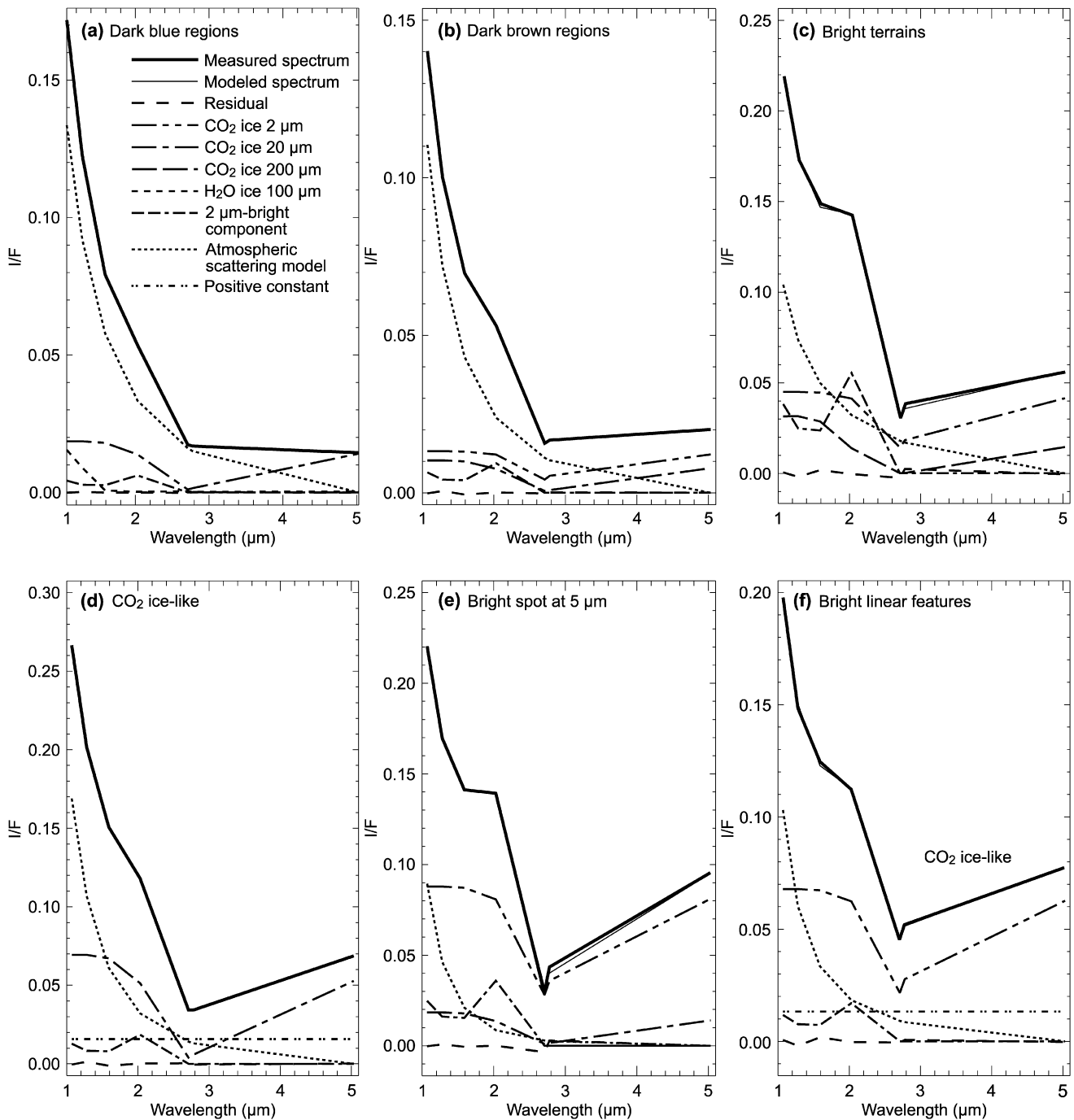


Fig. 8. Spectral Mixture Analysis on VIMS spectral endmembers using CO₂ ice spectra, a 100 μm grain size H₂O ice spectrum, the calculated bright component at 2 μm and an atmospheric scattering model. (a) Dark blue regions. (b) Dark brown regions. (c) Bright terrains. (d) CO₂ ice-like spectral endmember. (e) Tui Regio bright spot at 5 μm. (f) Bright linear features.

gions is modeled by CO₂ ices, the bright component at 2 μm and the atmospheric model. It has lowest I/F values at short wavelengths, which can be also explained by dark neutral spectral components at the surface. For the bright terrains (Fig. 7c), the atmospheric scattering contribution is still important at short wavelengths, but the CO₂ ice spectra and the bright component at 2 μm are used in significant proportions. The CO₂ ice-like spectrum is mainly modeled by a CO₂ ice spectrum and the atmospheric model, also with a contribution by

the bright component at 2 μm that improves the fit with respect to Fig. 4b. The bright spot at 5 μm (Tui Regio, Fig. 7e) is modeled with lower contribution by atmospheric scattering and a much higher contribution by CO₂ ices, which explains the high I/F values at 5 μm. This is consistent with an enrichment of the Tui Regio bright spot by CO₂ ice, as discussed for another 5-μm bright spot by Barnes et al. (2005). Finally, the bright linear features (Fig. 7f) are mainly modeled with CO₂ ices, a smaller amount of the bright component at 2 μm and, inter-

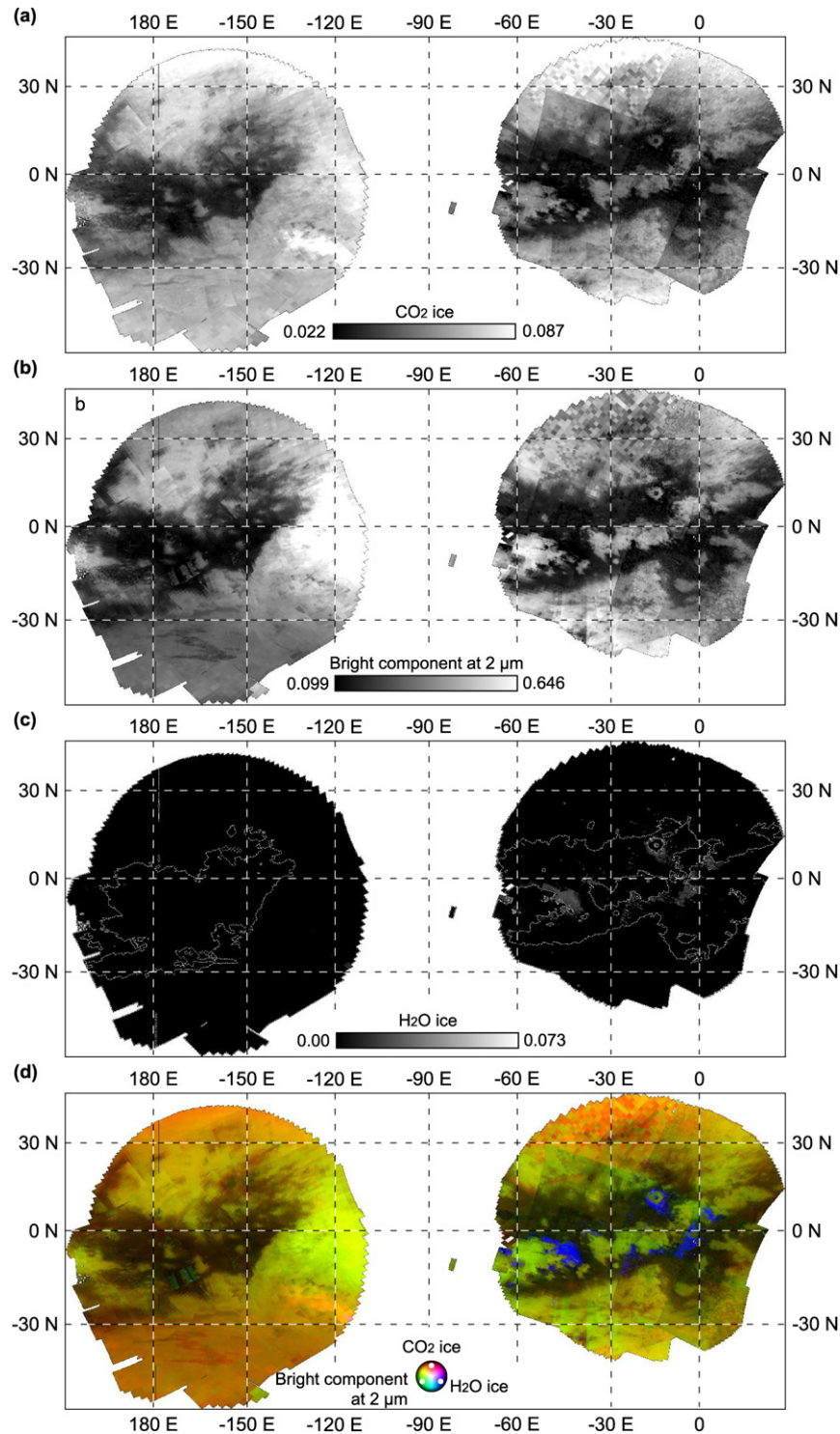


Fig. 9. Images of the unmixing coefficients for the three spectral endmembers related to the surface. (a) CO₂ ice. (b) Calculated bright component at 2 μ m. (c) H₂O ice, with a contour line at albedo = 0.08 (see Fig. 2b). (d) Color composite of the three endmembers: red = CO₂ ice; green = bright component at 2 μ m; blue = H₂O ice.

estingly, a significant proportion of a flat additive contribution at all wavelengths (constant part of the atmospheric scattering polynomial). This contribution occurs only on these features, which are present at the same latitude (about 30 deg. S) and have similar shape to clouds identified by [Roe et al. \(2005\)](#) and [Lellouch \(2006\)](#). In addition, these features are apparently transient, since they do not appear in the global map by [Barnes et](#)

[al. \(2007\)](#). As far as the SMA is concerned, the spectral components of clouds are treated the same as surface components. As detailed above, our spectral unmixing results show that the diverse spectral shapes of the VIMS Titan data can be best explained by linear mixtures of CO₂ and H₂O ices, a bright component at 2 μ m and a polynomial atmospheric scattering model.

3.5. Mapping of surface spectral units

The SMA was performed on the images using the same choices and constraints described in Section 3.4.4. The chi-square residual is lower than 1% for all the pixels. Mixing coefficients are displayed in Fig. 9.

The images of the unmixing coefficients shown in Figs. 9a–9c reveal sharp spatial features that are strongly correlated to albedo, because the wavelength channels are correlated to one another. As a consequence, bright areas are often the brightest regions at all wavelengths, thus all the spectral components have a higher absolute contribution. In addition, correlations of CO₂ ice and the bright material at 2 μm with albedo may be explained by the large proportion of VIMS spectra that have both lower *I/F* values in the double atmospheric window at 2.7–2.8 μm, and high values at 2 μm, respectively. There are exceptions, however, since the Tui Regio bright spot and the highest latitude regions correspond to the highest CO₂ ice mixing coefficients (Fig. 9a). The map of the bright component at 2 μm (Fig. 9b) also shows some structure, including a maximum east of Shangri-La and lower values in the northern bright terrain. In addition, the sharp edges between bright and dark areas indicate their spectral components are in fact due to surface materials. Water ice (Fig. 9c) is distributed in a few patches that correspond to the dark blue regions, as reported by Soderblom et al. (2007), including in the low-albedo areas surrounding the Sinlap crater.

Fig. 9d is a color composite that summarizes the unmixing coefficient images of the three spectral endmembers for the surface materials. Pure colors indicate the location of the purest compositions. CO₂ ice is in red, and is purest in the bright linear features, according to the SMA. The component bright at 2 μm is coded in green and does not appear as a pure component in any individual spectrum. The water ice is in blue, and the highest proportion occurs in the dark blue regions at the south–east edges of the bright terrains. However, because the image of the water ice endmember has been stretched, bright blue also corresponds to mixtures with CO₂ ice and the bright component at 2 μm (Fig. 9a), while dark indicates a low contribution by CO₂ ice, H₂O ice and the bright component at 2 μm (Fig. 9b). As a consequence, the intermediate color yellow (the Tui Regio bright spot at 5 μm, several areas south of Shangri-La, an area at the north of Shangri-La and several patches south of Fensal) are mixtures of CO₂ and the bright component at 2 μm.

The atmospheric scattering component (Fig. 10) is ubiquitous and plentiful, its minimum value occurring about halfway between zero and the maximum coefficient among all endmembers (Fig. 10a). In Fig. 10b, the image dynamic range has been stretched to enhance contrast. The image looks fuzzier than the other spectral components, indicating more gradual transitions between bright and dark regions. These observations are consistent with atmosphere-related phenomena. At some locations in dark areas, the atmospheric model shows slightly higher values than in the surrounding regions, especially near the edges with bright areas, implying a greater contribution at short wavelengths. These are regions where the presence of water ice has been previously suggested (Soderblom et al.,

2007). Given the few usable spectral channels VIMS provides for observing Titan's surface, this spectral shape is consistent with either atmospheric scattering or large-grain solid H₂O (or both). Thus, while H₂O ice may be present, the model does not specifically require its spectrum to explain the spectral shape of dark regions. Fig. 10c shows the constant term of the polynomial atmospheric model. A few areas require this constant in the model. They form coherent units that may indicate common properties of the materials. Three stripes at the south of Shangri-La correspond to the bright linear features (Fig. 2, arrow 5 and Fig. 8f), and a few patches with more random shapes are visible at the south east of Fensal. The presence of the constant term in the model indicates a spectral behavior that is different from most of the surface materials. Assuming the transient bright linear features are clouds, the other bright areas in Fig. 10c may have a similar origin.

3.6. Conclusions and perspectives on the Spectral Mixtures Analysis

The results from the SMA show more spectral variety in the bright than in the dark areas. The presence of two types of bright materials is corroborated both by the unique shape of the Tui Regio bright spot, which seems to be enriched in CO₂ ice compared to other areas, and by spectra of the other bright terrains. This diversity in the bright regions and the unusual spectral properties of the Tui Regio region are part of our earlier findings (McCord et al., 2006a). As discussed above, the bright linear features are likely clouds. With this hypothesis their apparent enrichment in CO₂ ice is enigmatic, since the extremely low saturation vapor pressure of CO₂ in the cold lower troposphere should preclude its incorporation in clouds higher up. If it is confirmed the linear features are clouds, their apparent enrichment in CO₂ is likely an artifact due to inadequacies in our atmospheric model, which causes the SMA to overestimate CO₂ contributions where atmospheric effects are different from other locations due to altitude.

On the dark terrains, the VIMS spectral shapes can be mainly explained by an atmospheric scattering model, plus relatively small amounts of CO₂ ice and the unknown bright component at 2 μm. Thus, removing the atmospheric contribution, the surface composition of dark terrains is probably dominated by a neutral spectral component. The dark blue areas imaged by VIMS are modeled with the same spectral components as the other dark regions, plus a small but significant fraction of H₂O ice with grain size about 100 μm. This H₂O ice distribution derived from the SMA is consistent with previous studies (Griffith et al., 2003; McCord et al., 2006a; Rodriguez et al., 2006; Soderblom et al., 2007), but we infer smaller areal coverage than implied earlier. Confusion of the water ice component with the atmospheric scattering component may at least partly explain this discrepancy. Indeed, higher *I/F* values at 1.0 μm than *I/F* values at 1.3 μm are common to the λ⁻⁴ contribution of the atmospheric scattering model and large-grain sized H₂O ice spectrum, which may increase the uncertainty in water ice detection.

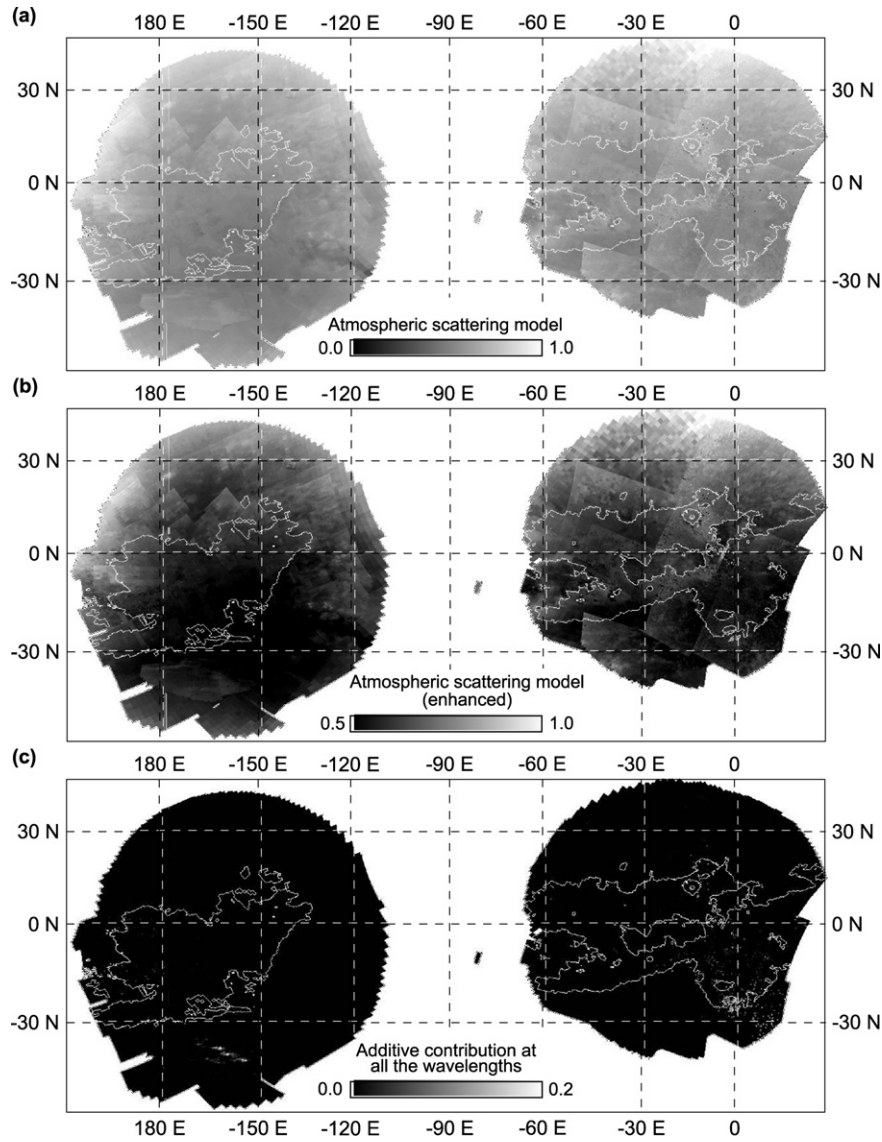


Fig. 10. Images of the atmospheric scattering contributions derived from the SMA with a contour line at albedo = 0.08 (see Fig. 2b). (a) Sum of all the atmospheric contributions. (b) Enhancement of figure showing structures over the dark areas that could be associated to H₂O ice at the surface. (c) Atmospheric contribution (constant term in the polynomial function) showing the different nature of the bright linear features at the South of Shangri-La, and some other areas southeastern of the Fensal region.

Our analysis confirms that spectrally distinct units exist on the surface of Titan. The mid-latitude surface diversity can be modeled using only three main spectral components plus H₂O ice, to a lesser extent. These results are compatible with the early analysis of the T_a data set (McCord et al., 2006a) and with the interpretation by Barnes et al. (2007), who also found a limited number of terrain types with a comparable description based on color composite images.

CO₂ ice spectra account for a large fraction of bright areas, and may explain the high I/F values at 5 μm of the Tui Regio bright spot. Although Hartung et al. (2006) placed an upper limit of 7% on the spatial coverage by pure CO₂ ice in Titan's bright surface regions, their observations were limited to longitudes where we find lower relative abundances of this endmember, which appears highly correlated with albedo (Fig. 8a). As noted by those authors, Tui Regio is absent from their obser-

ations. Additionally, intimate mixtures with other compounds (e.g., H₂O ice) could reduce the strength of the absorptions (2.01 and 2.07 μm) used in the search, artificially lowering the derived upper limit on abundance. We discuss possible absorption features in detail in Section 7. In dark regions, atmospheric scattering accounts for most of the signal, suggesting the surface is composed of a (dark) spectrally neutral material, which is consistent with the findings of McCord et al. (2006a). However, the shape of the calculated bright spectral endmember at 2 μm is somewhat mysterious, since it is not a characteristic of any of the materials supposed to be present on Titan. However, the spatial distribution of this endmember does suggest it is related to the surface. A similar component has been observed by Rodriguez et al. (2006) as a specific unit near the Huygens landing site. In this study, we show that this endmember contributes in most of the bright terrains. The spatial distribution and the

spectral shape of this component do not provide sufficient information to identify a related composition. The interpretation of spectra in these areas should also be investigated in parallel with information on the morphology and state of the surface provided by other instruments (e.g., radar).

We propose here a spectral interpretation of the different units, including areas composed of almost pure components, and regions where two or more of these components are mixed. Our analysis further suggests that the SMA approach might be used to detect and map atmospheric scattering contributions, which are relatively higher than the other components above the blue unit. These results may be used to constrain more rigorous models of atmospheric scattering (e.g., Griffith et al., 2003; McCord et al., 2006b, 2007; Rodriguez et al., 2006; Ádámkóvics et al., 2006). On the other hand, a more accurate (i.e., physically-based) atmospheric model would be a valuable improvement to the present SMA.

4. Spectral features search above the noise level

The second approach we used for investigating the surface composition of Titan with the VIMS data was to search within the methane windows discussed earlier (Fig. 1) for spectral features that might be associated with the surface materials. We used several methods to search for spectral features, and, in the process, explored the noise characteristics of the VIMS data. We concentrate on the 5- μm spectral window because it is the spectrally widest (~ 15 spectral channels) and is least affected by atmospheric scattering, but we also investigated the other methane windows.

First, we analyzed the spectral units identified in the previous section for each of the VIMS data sets (Tables 1 and 2; Figs. 2–4). The simplest approach is to average the spectral segments within the usable windows, first for the entire scene, and then for the pixels classified as each of the three main spectral units identified in Fig. 4b: CO₂ ice, 2- μm bright, and atmospheric

scattering (plus water ice). The average 2- and 5- μm window spectra for each of the three spectral units are shown in Fig. 11. These are calculated using for each pixel spectrum a weighting factor that is a function of the mixing coefficient for each of the three spectral units. The spectrum for each pixel in each image is scaled to the average (of all 980 images used in this study) to remove overall spatial variations in brightness, and variations between images. The spectra are quite noisy due to the low signal (Table 1), and show considerable evidence of instrument effects, especially noise spikes and erratic darks (see discussion below). None of these plots shows any spectral feature above the noise level (dashed lines = one standard deviation), which is controlled by the low signal in this spectral region and the several instrumental effects present. The small features present in the spectra in Fig. 11 can be associated with individual detector performance characteristics and are not properties of Titan. This result is consistent with but considerably extends the initial search of this spectral window made earlier (McCord et al., 2006a), with more recent results reported by McCord et al. (2006b, 2007).

While we focus in this section on the 5- μm window, we also conducted a search for spectral features within the other five spectral windows in a similar manner. Only the 2- μm spectral window seems clear and broad enough (~ 5 spectral channels) to perhaps reveal a feature. The 2.8- μm window is broad enough but it is complicated by an unidentified absorption near its center, discussed in some detail from VIMS by McCord et al. (2006a, 2006b) and using Earth-orbital telescope by Coustenis et al. (2006), and the other, shorter wavelength windows, are both very narrow (1–2 channels) and affected more seriously by the haze.

Note that both the spectra for the 2- and 5- μm windows for the atmospheric scattering-like unit show elevated I/F values at the edges of the spectral windows (less overall methane absorption) when compared to the other units. This is consistent with the association of this endmember with atmosphere effects

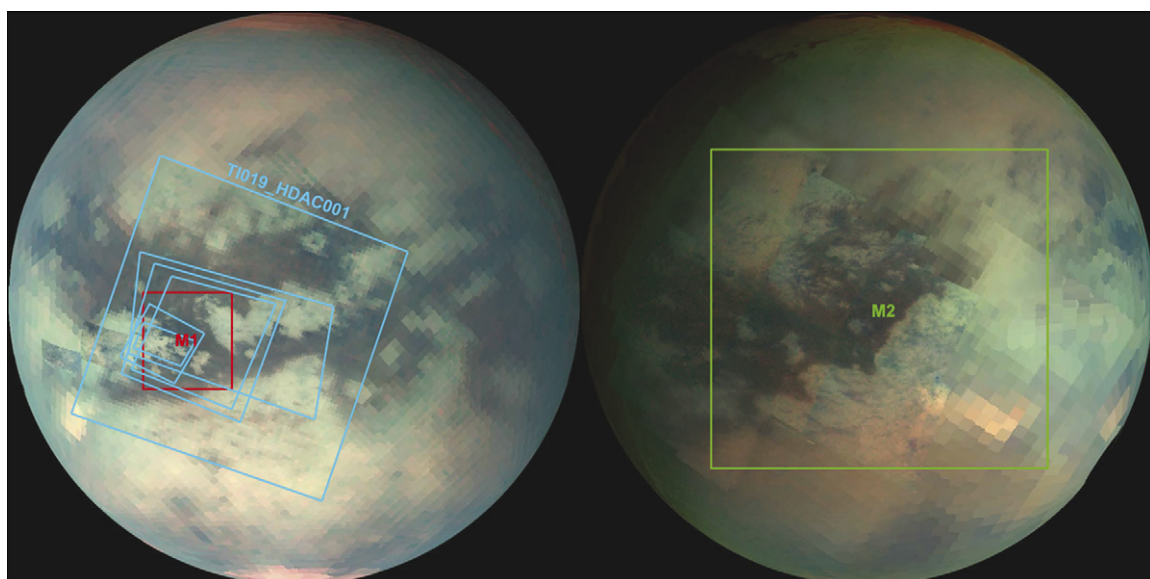


Fig. 11. Shown here is the general location on Titan of the data sets used for the search for absorption features within the methane windows (Table 2).

(as discussed in the previous section), since the atmospheric path-length would be reduced in this case. As a comparison, spectral segments taken near Titan's limb, where the signal is almost exclusively due to the atmosphere, are nearly flat across both windows.

5. Search for spectral features within the global noise level

With no spectral absorption features appearing above the whole-scene noise level for scenes so far analyzed, it remains possible that there exist features too weak to appear in these data of relatively low signal-to-noise ratio (see the signal levels noted in Table 1). A search for such features must involve an analysis of the noise characteristics of the data as well as an analysis of the spatial distribution of any suspected features.

In particular, we searched for absorption features that satisfy any or all of the following criteria: (i) The feature is apparent in the average of all pixels in a dataset (provided dark and flat-field corrections are accurate to a specified degree). (ii) Contiguous subset(s) of an image contain a higher concentration of pixels showing the feature than predicted by the data noise statistics. This excess should be observed consistently in different images containing the same region in question. (iii) The feature is spatially correlated with a morphologically and/or spectrally distinct unit, again consistent from frame to frame of the same area. Using these criteria, we reduce selection bias, which can result from choosing pixels based on their adherence to the proposed spectral shape.

For this search, we selected a mosaic of VIMS data sets (Jaumann et al., 2006) because it covers a region of special interest. For example, the existence of weak spectral features in the VIMS data set for this region has been suggested recently (Clark et al., 2006a, 2006b, 2007). The mosaic covering this re-

gion is TI019_HDAC001, which is described in Table 1. The locations of the datasets described in this section are shown in Fig. 12.

We followed Clark et al. by using the central region (161×171 pixels) of the T1_019_HDAC001 cube (Fig. 13a) was analyzed for the standard deviation, which is plotted (± 1 SD) as dashed lines above and below the average (Fig. 13b). This prevents overall pixel-to-pixel brightness differences from distorting the spectral variance. There are two anomalies in the average spectrum and the one-standard-deviation envelope in Fig. 13b, at the 4.94- and 5.09- μm channels, which are due to noisy detectors, as discussed below. No obvious Titan spectral features appear.

We then analyzed the scene, spectral channel by spectral channel. New brightness-scaled image cubes were made, excluding each of the selected test spectral channel image planes, and then the I/F values in the test channel were compared to the average and standard deviation shown earlier (Fig. 13b). Pixels with I/F deviations for each of the test channels were flagged using 0.5, 1, 2, and 4 standard deviations as criteria. They were also distinguished as being either positive or negative deviations. Since the average spectrum is relatively smooth and featureless, any real absorptions at the pixel level will appear as negative deviations from this mean. As described above in our search criteria, an excess of negative deviations, and/or a spatial clustering of outlier pixels, would suggest such an absorption (or potentially an emission) feature. Fig. 14 shows maps of pixels with positive (white) and negative (gray) deviations beyond the one-standard-deviation criterion for three spectral channels. One can see in Fig. 14 the outlines of the frame boundaries making up the mosaic image due to differences in signal levels and noise characteristics among the mosaic composite frames. The spatial distribution of the positive

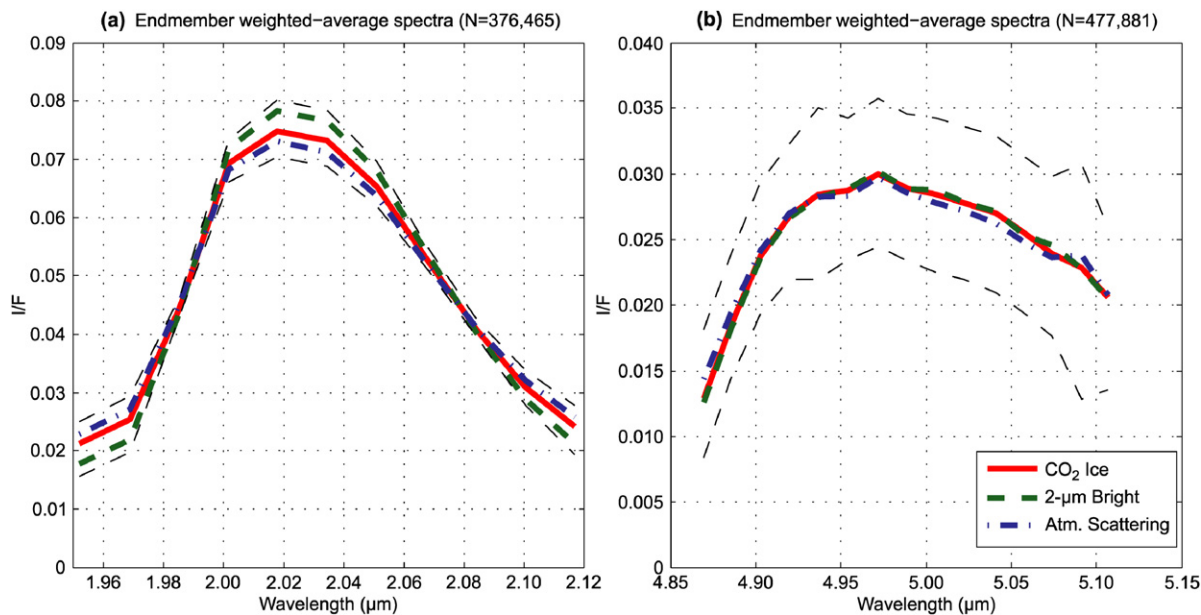


Fig. 12. Plots of weighted average spectra for each of the five spectral endmembers found by SMA, for 272 data cubes. For each endmember, we show (a) the 2- μm window average spectrum, and (b) the 5- μm window average spectrum. Dashed lines indicate one standard deviation from the mean. We note a relative broadening of the spectra associated with the atmospheric scattering-like endmember, for both windows, consistent with its hypothesized atmospheric origin. We also note that no spectral obvious spectral features are present.

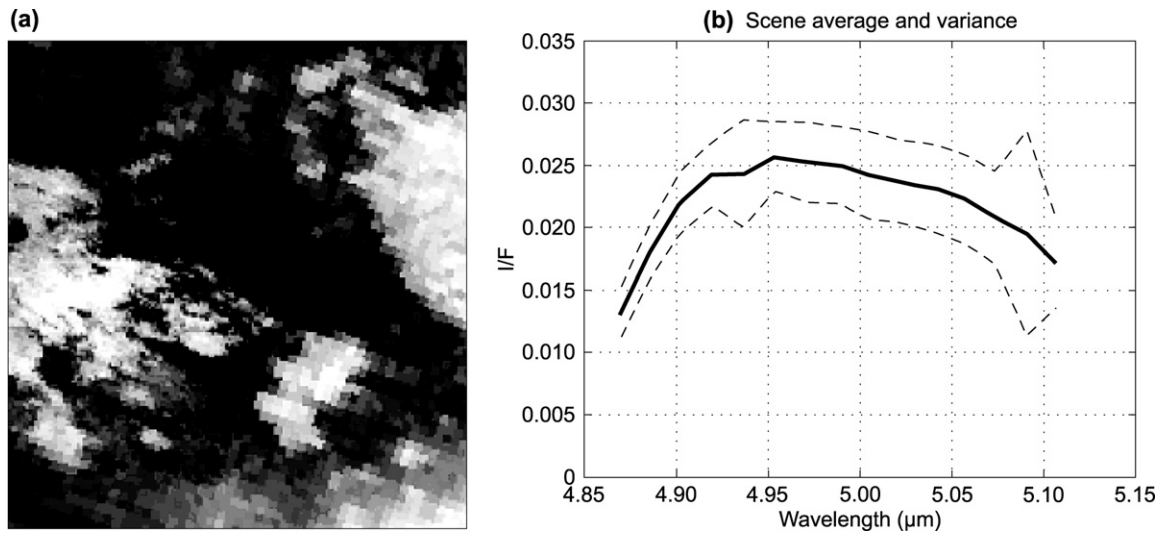


Fig. 13. The central portion of mosaic TI019_HDAC001 (161×171 pixels) is shown on the left and the average spectrum with a one-SD envelope (dashed lines) is shown on the right, calculated as described in the text.

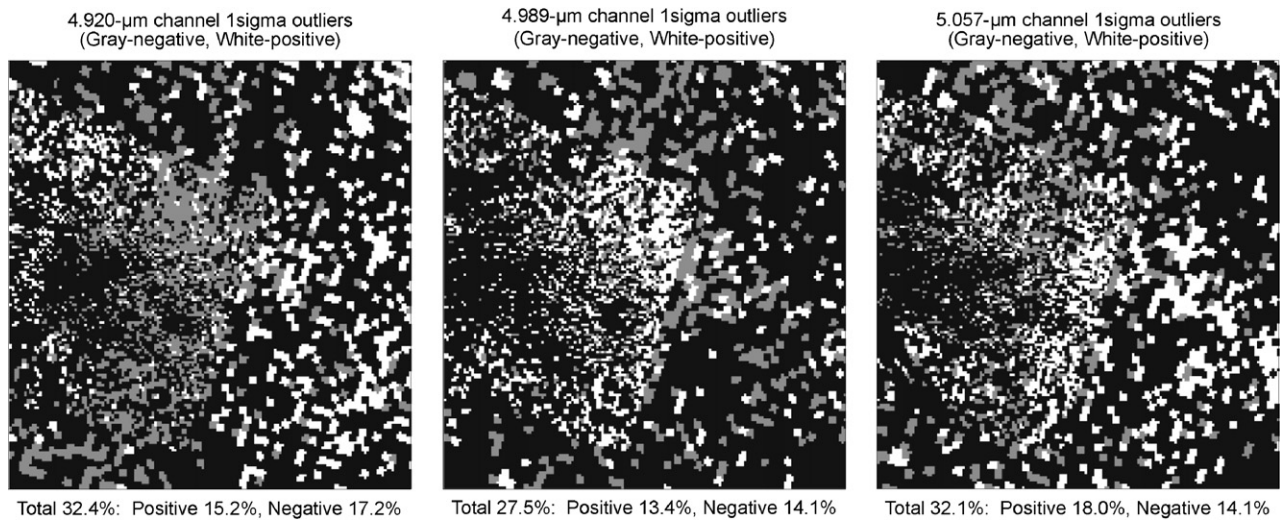


Fig. 14. Outlier pixels, defined as those deviating from the whole-scene mean spectrum by >1 SD, for three different channels: 4.92, 4.99 and 5.06 μm . Gray pixels are negative outliers, and white pixels are those deviating in the positive direction.

and negative deviations does not seem to us to show a discernable pattern, except that darker regions tend to have more deviations (positive as well as negative) because of the lower signal and SNR for lower albedo regions.

Fig. 14 shows that the number of pixels with one-SD deviations is nearly what would be expected if the noise were Gaussian. For each of the three test channels (4.820, 4.989 and 5.057 μm), the percentage of pixels with total, positive and negative deviations are, respectively, 32.7, 15.2 and 17.2%; 27.5, 13.4 and 14.1%; and 32.1, 18.0 and 14.1%. Gaussian statistics predict that the total number of deviations would be 31.7% and the percentage of pixels with positive and negative deviations would each be half this.

We then looked for spectral features in each and every spectral channel in the window. Each of the four plots in Fig. 15 shows 15 average spectra. Each spectrum is the average of all pixels in mosaic M1 with a deviation (positive or negative) at

a selected spectral channel greater than $1/2$, 1, 2, and 4 standard deviations. There are 15 spectral channels used in the 5- μm window analysis here and so there are 15 average spectra in each of the four plots in Fig. 15. None of these average spectra shows a spectral feature different than in the average for the scene (Fig. 12b), except that for large deviations, especially for 4 SD, incompletely corrected noise spikes become evident as positive (but not negative) deviations for each and every channel (Fig. 15, lower right). The exception is the noisy detector at 5.09 μm , the erratic behavior of which will be discussed thoroughly in Section 8.

To better show that the noise characteristics of this VIMS data set are nearly Gaussian, Fig. 16 shows a plot of the number of pixels with outliers (deviations) of different magnitudes (measured in numbers of standard deviations) for each of the 15 spectral channels in the 5- μm window. The total number of outliers at each deviation level is shown as solid lines, the number

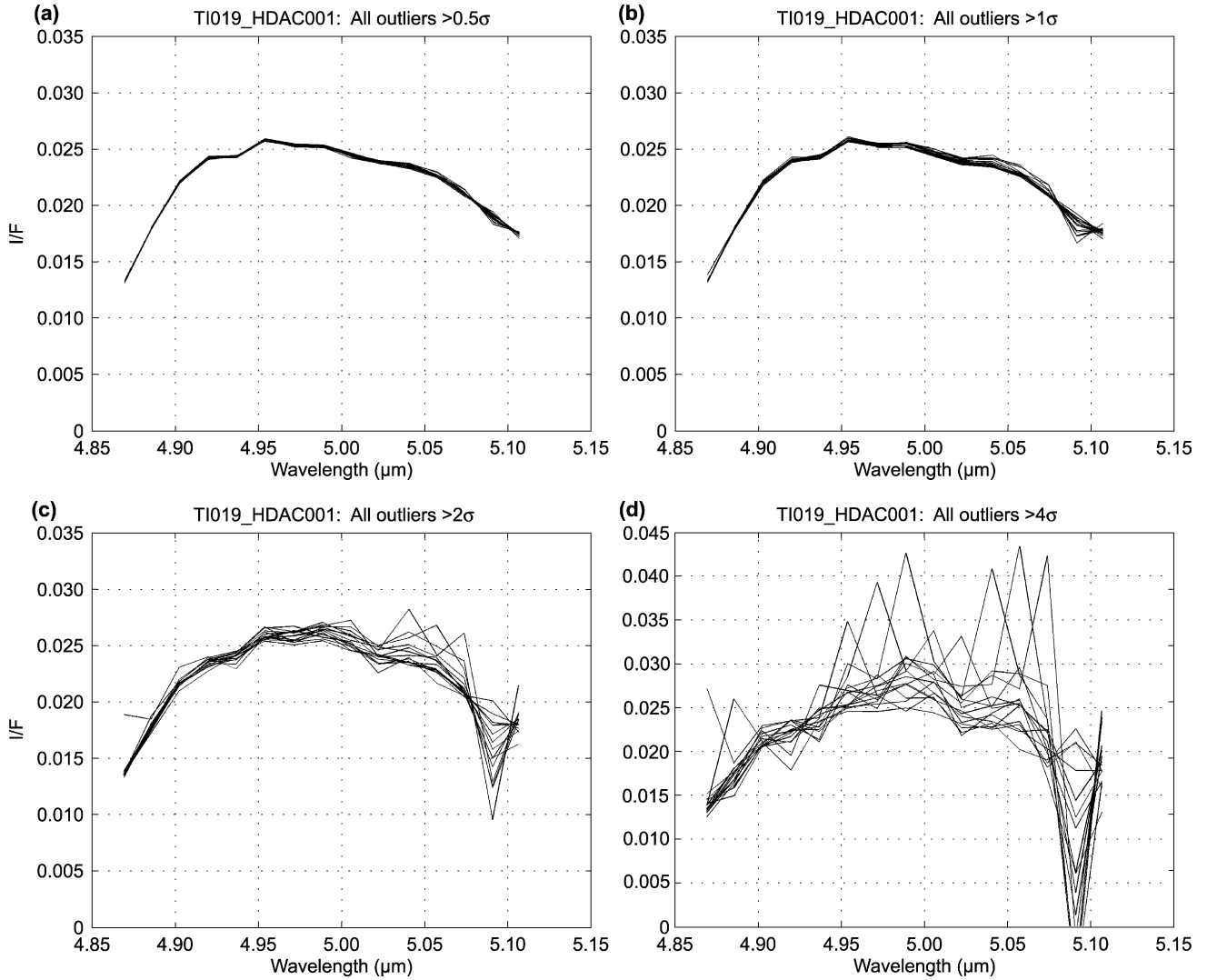


Fig. 15. Average 5- μm spectra for all outlier pixels (deviating in the positive or negative direction) for thresholds of 0.5, 1.0, 2.0, and 4.0 times the whole-scene standard deviation. Each line is the average outlier spectrum for one channel in the 5- μm window.

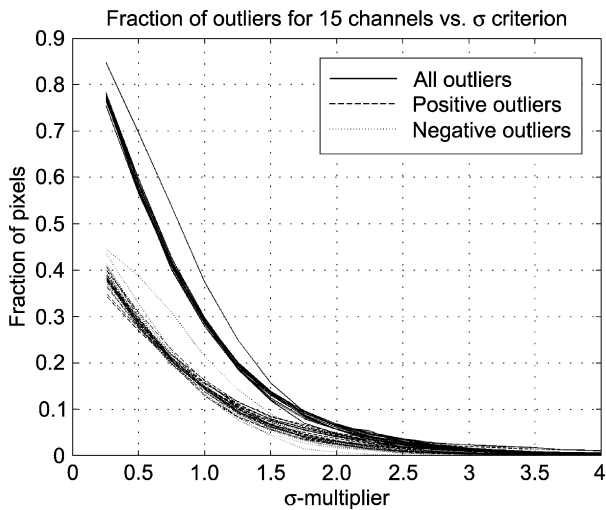


Fig. 16. The Gaussian nature of the VIMS data are shown here, by plotting the fraction of pixels in a scene deviating by some multiple of the standard deviation. A true Gaussian distribution would have ~ 0.16 of pixels deviating in both the positive and negative direction by >1 SD.

of positive outliers as dashed lines, and the number of negative outliers as dotted lines. There are 15 plots for each of total, positive, and negative deviations, one for each spectral channel. As a comparison, note that for Gaussian statistics, the number of 1-SD outliers is predicted to be 31.7%, which is near where the 1- σ totals lie in Fig. 16, except that there are a few more due to incompletely corrected noise spikes, as shown also in Fig. 15. Further, note that there is no excess of negative deviations over positive deviations, suggesting that there is no spectral absorption present beyond what might be shown in the scene average (Fig. 12b) (against which the deviation is measured) hidden in the data near the noise level. The good news is that the VIMS data noise characteristics seem to be nearly Gaussian and thus are well-behaved, except for the noise spikes and a few noisy detectors (e.g., at 4.94 and 5.09 μm , see Section 8).

Having established the near Gaussian statistical nature of the VIMS data, we proceeded to analyze the pixels with positive and negative deviations separately. In Fig. 17 we show (a) an average of spectra for pixels with one-channel *negative* (only) deviations $>1\sigma$ at spectral channel 4.973 μm and (b) average

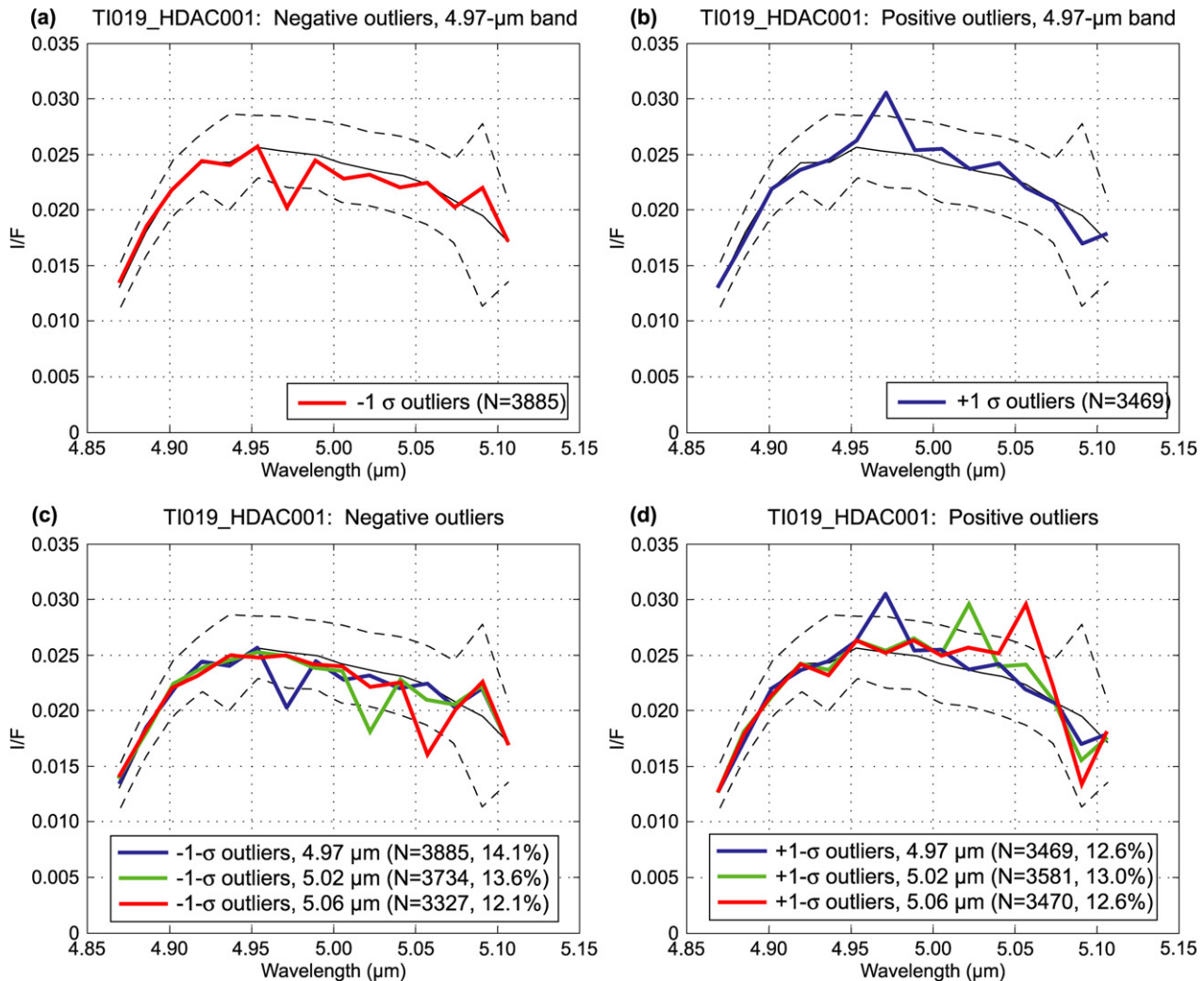


Fig. 17. Average 5- μm spectra are shown for >1 SD outlier pixels for (a) negative deviations at 4.97 μm , (b) positive deviations at 4.97 μm , (c) negative deviations at 4.97, 5.02, and 5.06 μm , and (d) positive deviations at 4.97, 5.02, and 5.06 μm . The whole-scene average spectrum is shown in black, with a one-SD envelope (dashed lines).

spectra for pixels with one-channel *positive* (only) deviations $>1\sigma$. The average spectrum for the scene and the standard deviation envelope are also shown, taken from Fig. 12b. As shown in Fig. 16, for this scene there is approximately the same number of positive and negative deviations in the scene at each deviation magnitude, and thus we see both a negative (false absorption) and a positive (false emission) feature in Figs. 17a and 17b but there is no discernable spectral feature at 4.973 μm in the overall average spectrum for the scene. In Figs. 17c and 17d, we extend this analysis by showing positive- and negative-only deviations for three spectral channels [4.97 (as in Figs. 17a and 17b), 5.02 and 5.06 μm]. This plot suggests that false absorption and false emissions features can be found at each and every spectral channel if only pixels with negative or positive deviations are selected for averaging. Fig. 18 shows the same effect for each and all 15 spectral channels in the 5- μm window. Note again the noisy channels at 4.94 μm and 5.09 μm . Further, we find the same effect by selecting for negative and positive deviations that are more than one channel wide and that have arbitrary spectral feature shapes, but there are of course fewer

pixels with broader or more complicated deviations, according to Gaussian statistics (McCord et al., 2006b, 2007). This exercise demonstrates that one can show negative (false absorption) features or positive (false emission) features by selecting pixels with only negative or positive noise deviations. This effectively is what is done in some analysis techniques used to search a data set for a pre-assumed absorption or emission feature at a signal level near or below the noise level.

In summary, we present and demonstrate here a simple but thorough and unbiased analysis approach for searching for slight excesses of negative (positive) deviations in the data that might suggest an absorption (emission) feature slightly below the noise level of the data. After a detailed analysis of the VIMS IR data for the mosaic data set TI019_HDAC001, we find no evidence of spectral absorptions at any spectral channel or contiguous groups of channels in the scene average spectrum nor any evidence of such absorptions for specific pixels significantly above the number of pixels predicted by Gaussian statistics. The pixels associated with negative (and positive) deviations from the mean spectrum seem uncorrelated with fea-

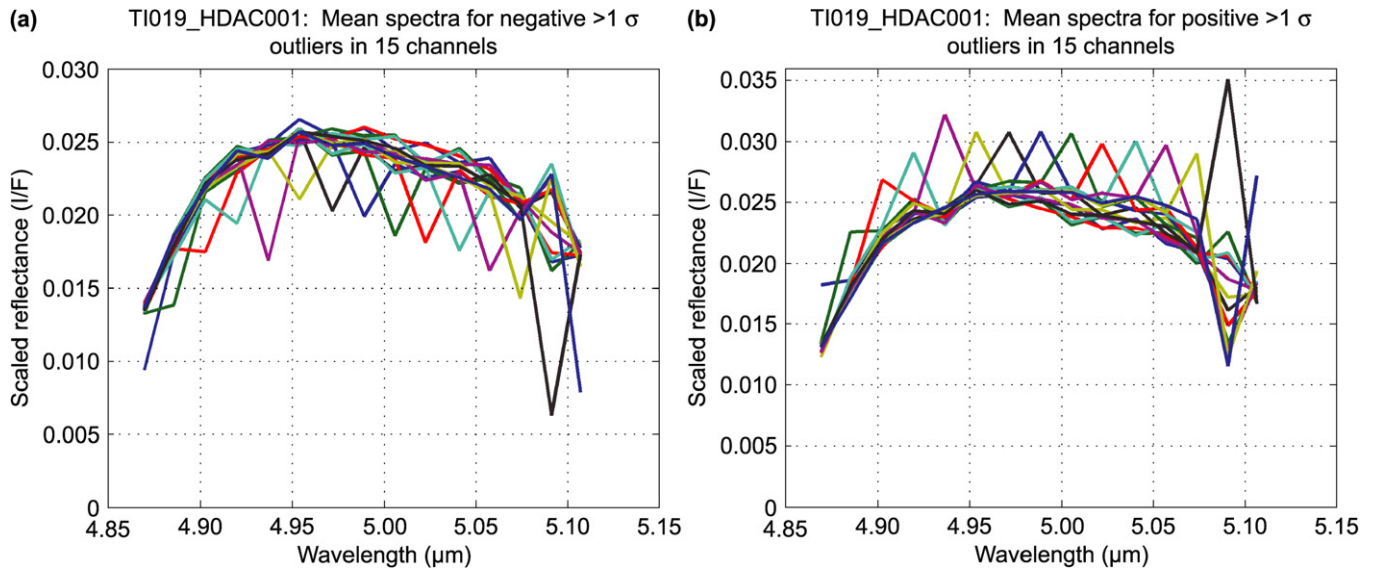


Fig. 18. Average 5- μm spectra are shown for >1 SD outliers at each channel, for (a) negative deviations and (b) positive deviations.

tures in the scene except that there are more deviations (positive as well as negative) for lower-albedo regions because of the lower signal level in those regions.

6. Search for benzene

We specifically analyzed the same VIMS dataset (M1) for recently reported spectral features. Clark et al. (2006a, 2006b, 2007) recently reported detection of widespread aromatic and aliphatic hydrocarbon deposits on Titan using the VIMS data. We explored the data sets M1 and TI003_GLOBMAP001 (M2) that were used by Clark et al. as well as other data sets using our analysis approach described above in Section 5. We also attempted to fit a laboratory spectrum for benzene plus carbon black supplied to us by R. Clark and used in the Clark et al. study to VIMS spectra of Titan in the 5- μm window. In doing so, we followed the Tetracorder algorithm (Clark et al., 2003; Swayze et al., 2003) used in the Clark et al. study, except that “inverse” absorption bands are also allowed. Each VIMS spectrum (for each pixel) is first divided by a continuum, defined as a line fitting two (or more) points adjacent to the benzene band as it appears in the laboratory spectrum. The result is then matched (using a least-squares fit) to the laboratory spectrum (which has also been divided by its own continuum), in this case the spectrum of benzene plus carbon black. If the correlation coefficient meets some arbitrary threshold, positive or negative, the pixel is declared a match. Negative correlation coefficients indicate “inverse” absorption bands, or positive outliers. Positive and negative outliers are each mapped separately, and their mean spectra plotted along with the standard deviation for the whole scene, representing the noise level. We first treated the M1 mosaic.

Initially, we searched the data set for obvious absorptions by calculating the average spectrum (Fig. 19a) for only bright and only dark pixels (identified in Fig. 19b). By comparing these averages with the total scene average shown in Fig. 12b, we see that no spectral features appear other than due to the noisy

detector at channel 4.94 μm . We then fit the Clark laboratory spectrum for benzene plus carbon black to the spectrum for each of the pixels. We also tried to fit the inverse of the laboratory spectrum. The results are shown in Fig. 20. Pixels were found with both negative (Fig. 20a) and positive (Fig. 20d) spectral features matching the laboratory spectrum and its inverse. The average for all pixels with both positive and negative matches is shown in Fig. 20c, where a slight positive feature appears at the benzene band suggesting a slight (but probably meaningless) deficiency of absorption feature in the scene. The average spectrum for all positive and negative outliers is shown with the average spectrum for the entire scene in Fig. 20b. There are approximately as many positive as negative spectral feature matches found for this data set, suggesting no significant excess of pixels with the laboratory feature match above what is expected from the noise characteristics. There is an interesting tendency for the spectral channel on the long-wavelength side of the benzene band to be high when the benzene band channel next to it is low (and vice versa), and we suspect that there is some erratic behavior in the performance of this detector (see Section 8). The locations of the pixels with positive and negative feature matches are shown in Fig. 21. Again, no systematic association of the alarmed pixels with spatial features seems evident, other than a tendency for both positive and negative outliers (in approximately equal numbers) to be associated with lower-signal regions (that is, darker features). These results are similar to those found in Section 5 when using our less sophisticated spectral-shape search template (simple V- or Gaussian-shaped spectral feature rather than an actual laboratory absorption).

As a further test, we treated M1 using the same Clark laboratory absorption profile, but shifted the Clark benzene band profile to center on 5.005 μm (from 5.041 μm). We obtained similar results as by using the original band wavelength position (Figs. 22, 23). This result also is found by shifting to other wavelength positions. In all cases the alarmed pixels, positive and negative outliers, are concentrated in the areas of lower

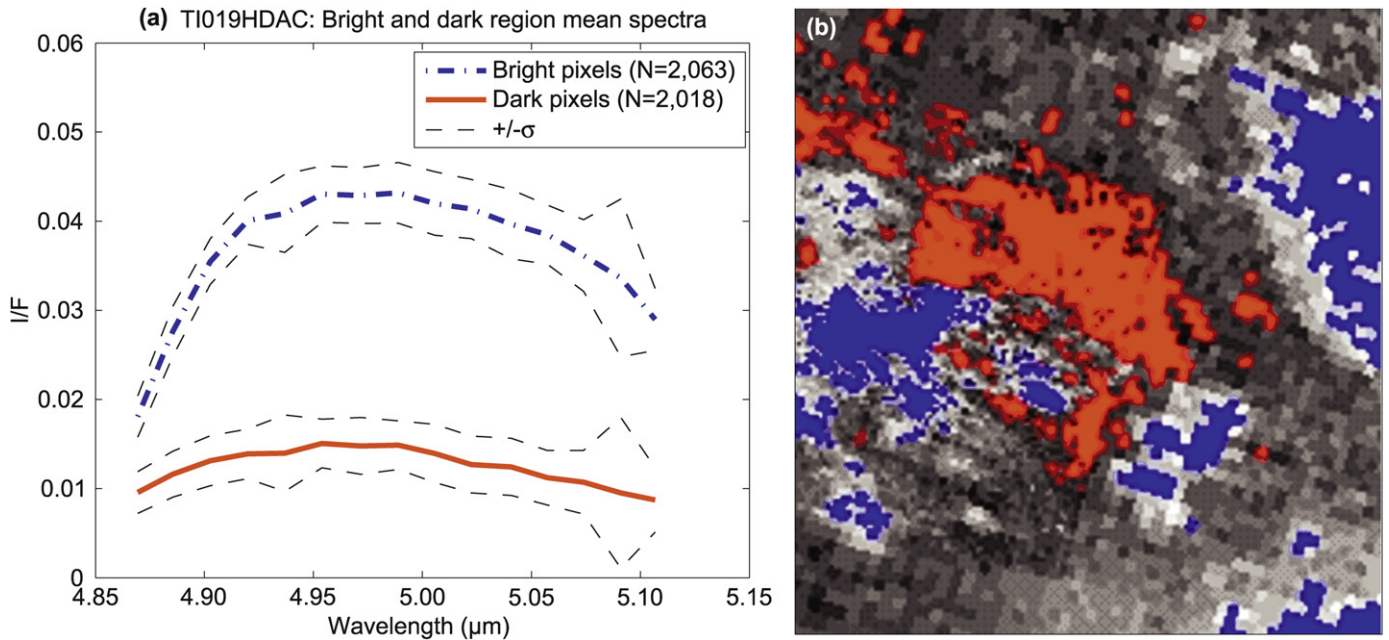


Fig. 19. Average 5-μm spectra are shown for the brightest and darkest ~3000 pixels in the TI019_HDAC001 mosaic subspace (highlighted in the adjacent plot), where brightness is defined as I/F in the 2.03-μm window.

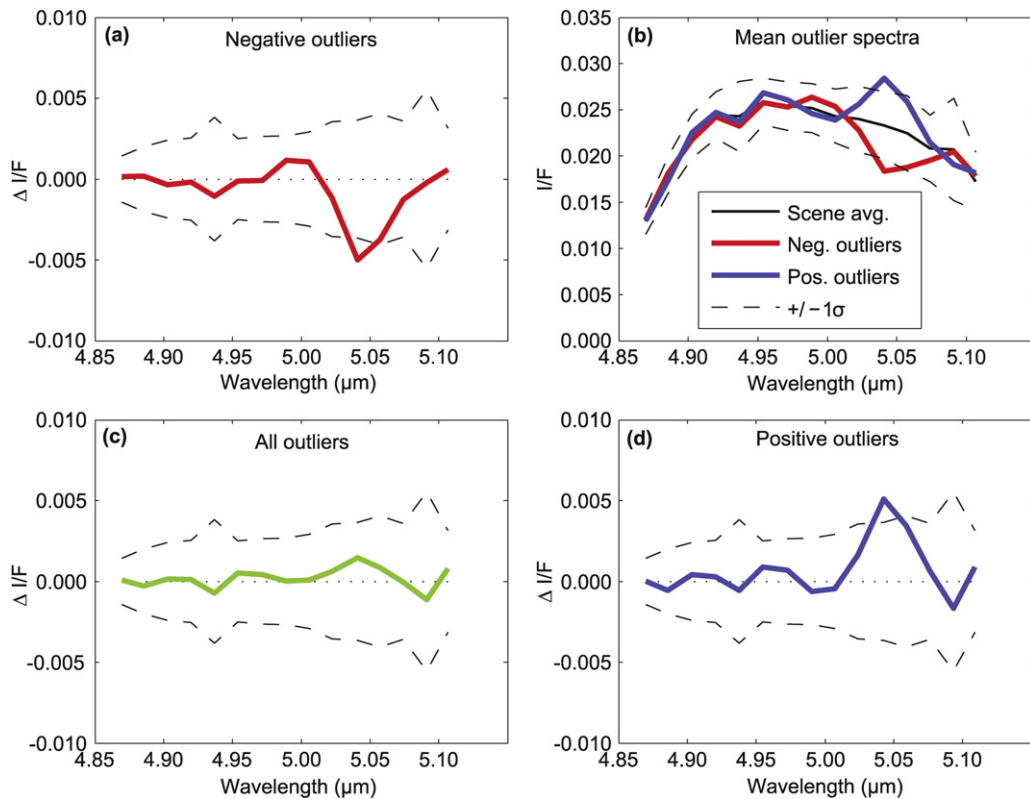


Fig. 20. Average 5-μm spectra are plotted for outlier pixels in the TI019_HDAC001 mosaic subspace, using the band-fitting approach described in the text, with a benzene + carbon black laboratory spectrum centered at ~5.04 μm. The average of pixels deviating in the negative direction is plotted in red, while the average of pixels deviating in the positive direction is plotted in blue.

SNR, namely darker regions, and occur in approximately equal numbers and according to Gaussian statistics.

Further, since M1 is a mosaic of the original VIMS data sets, and thus may contain artifacts from processing and resam-

pling, we analyzed the original VIMS data cubes from which the mosaic was made. We again searched for pixels with spectra matching the Clark et al. laboratory spectrum and its inverse. Fig. 24 shows each of the cubes covering M1, with the pixels

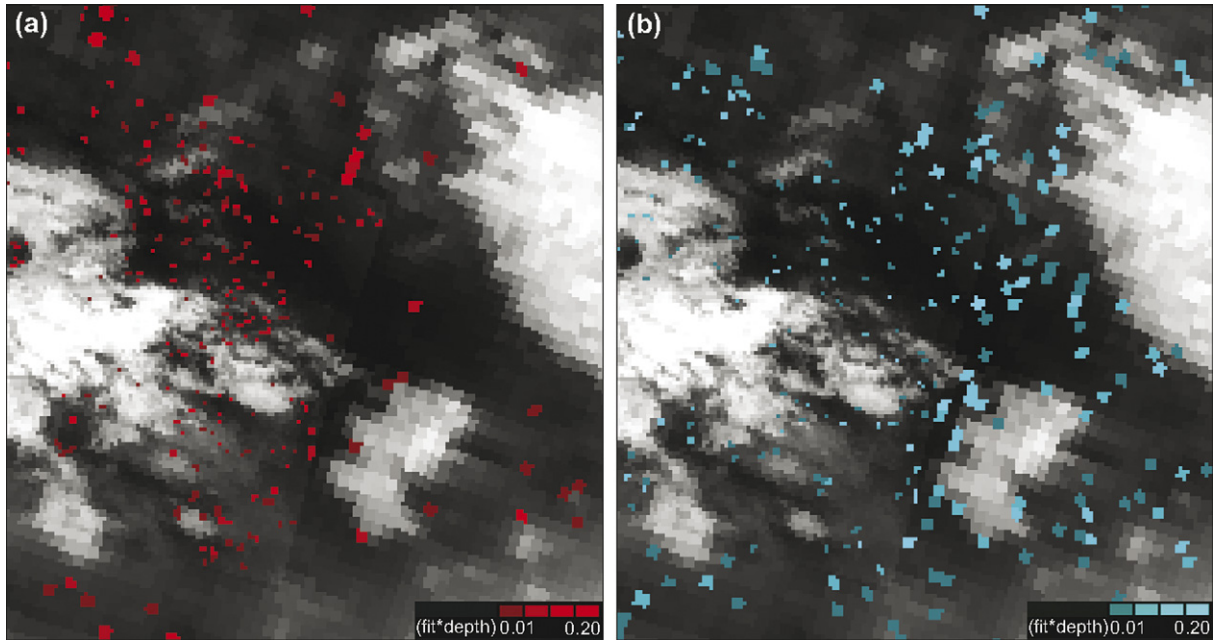


Fig. 21. A map of the outlier pixels at $\sim 5.04 \mu\text{m}$, using the same band-matching algorithm, and color coding as in Fig. 19.

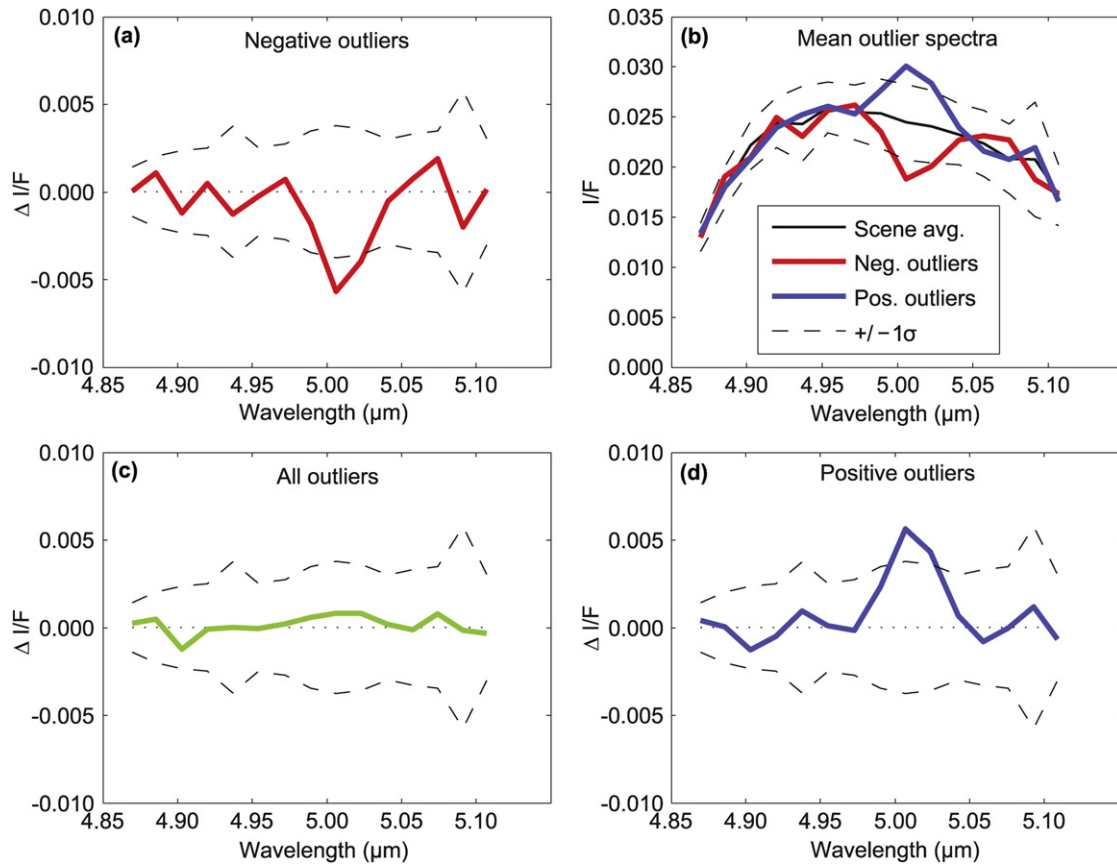


Fig. 22. The same plot as in Fig. 20, but with the band centered at $\sim 5.01 \mu\text{m}$.

alarmed that match the laboratory spectrum (red, middle row) and its inverse (blue, bottom row). Interestingly, there is little consistency in the exact pixels alarmed among the VIMS data sets covering the same spatial scene, i.e., the same location does

not match the laboratory spectrum consistently from data set to data set for the same scene.

We also searched the VIMS data sets treated in our search for spectral diversity described in Section 3 (Fig. 2 and Table 1)

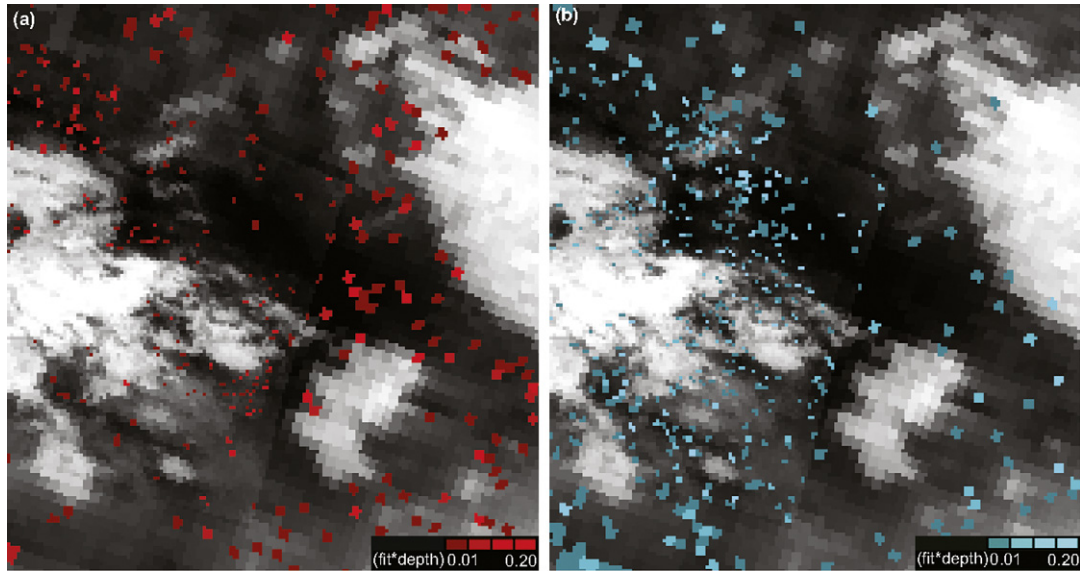


Fig. 23. The same plot as in Fig. 21, but with the band centered at $\sim 5.01 \mu\text{m}$.

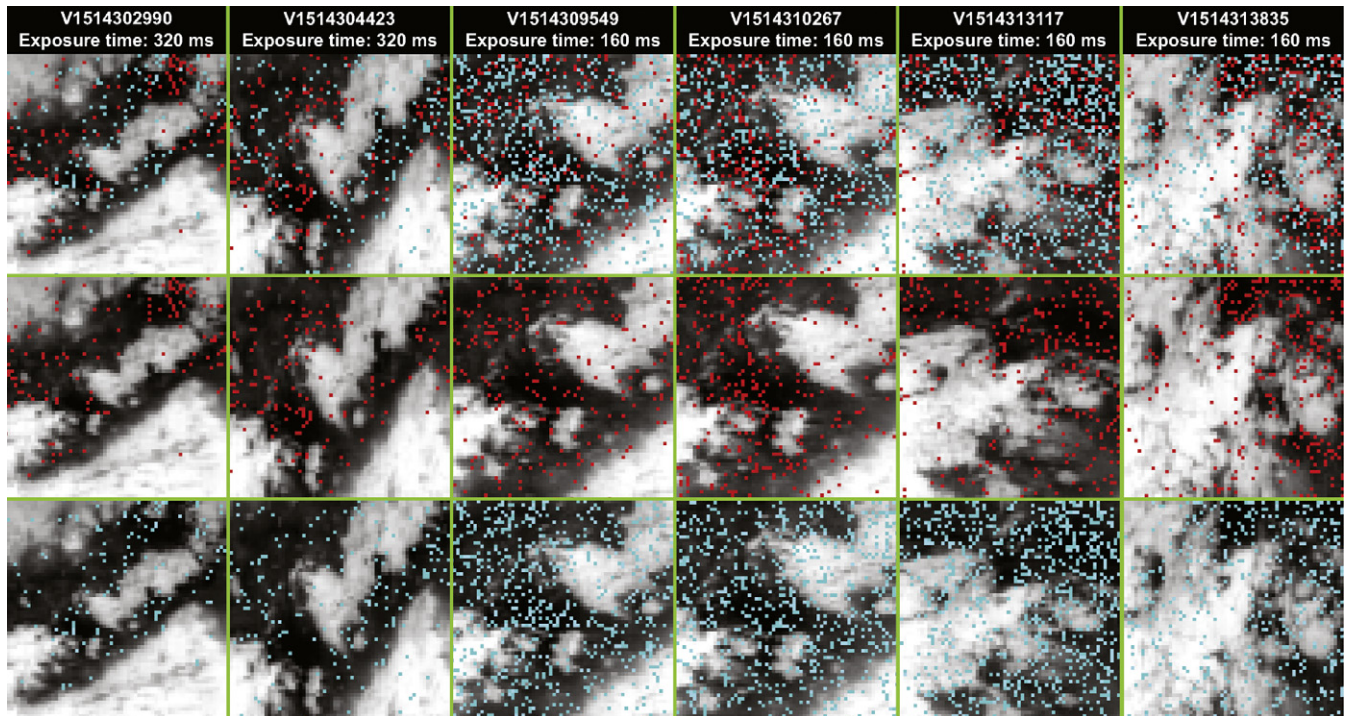


Fig. 24. Band-fitting results for individual data cubes making up the mosaic TI019_HDAC001, using the same laboratory spectrum as in Fig. 20, at $\sim 5.04 \mu\text{m}$. Again, red pixels are matches in the negative direction from the mean, while cyan indicates pixels deviating in the positive direction. Note the inconsistency in geographic location of the matching pixels. The $|\text{IFIT} \cdot \text{DEPTH}|$ criterion is >0.1 for the darker shade, and >0.2 for the brighter shade of each color. The total number of positive outliers is 2359, while the total number of negative outliers is 1393.

for the benzene feature using the same technique and found no evidence of the feature.

7. Analysis of other scenes

7.1. Search for absorptions

Following the above analysis, we treated the data set TI003_GLOBMAP001 (M2, Fig. 25; Table 1), which is of

higher SNR than the other data sets treated here and covers an entirely different region of Titan. Again, the Clark et al. laboratory spectrum and its inverse were used in an attempt to find pixels with matching spectra, which are encoded as red (lab) and blue (inverse lab) (Fig. 25). Again, no pattern of alarmed pixels is evident, except for a cluster of laboratory spectrum matches (red) in the upper-left region, very near the limb. A closer inspection of some of these pixels clearly shows noise spikes (positive noise features) in the $5.09\text{-}\mu\text{m}$ channel,

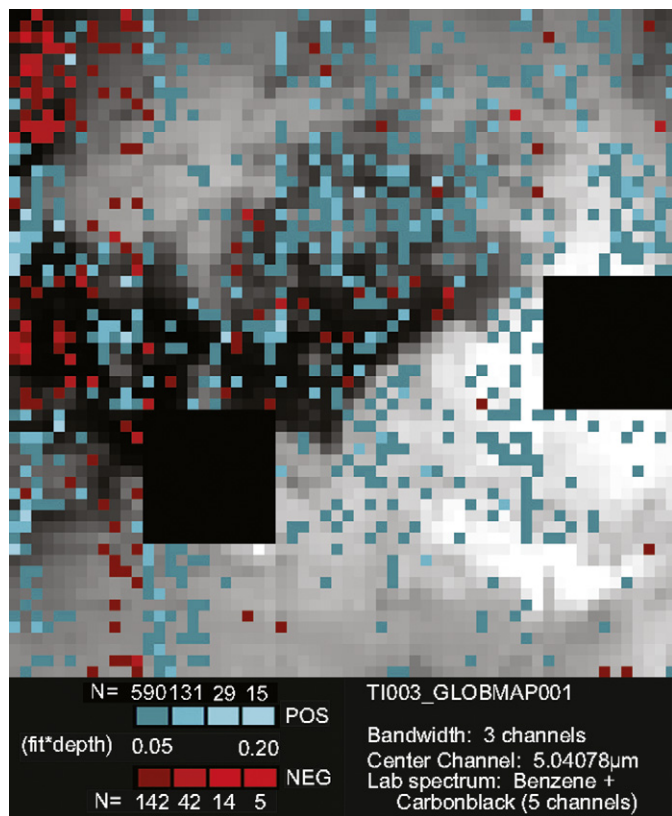


Fig. 25. As in Fig. 24, we plot the pixels matching an absorption at $\sim 5.04 \mu\text{m}$, this time for the data cubes used in the mosaic TI003_GLOMAP001_1.

which tends to create a false negative feature shortward of that channel. In subsequent analyses, the cluster at upper-left was not found to be present in other VIMS datasets containing the same geographic region of Titan. We therefore conclude that this feature is likely an artifact, enhanced by the low SNR in that region.

Using the un-mosaicked image cubes listed in Table 1, we conducted a search for any excess of negative deviations from the scene mean spectrum at each and every spectral channel in the $5\text{-}\mu\text{m}$ window, following our procedure discussed in Section 5. In sequence S15 (T17) we found one spectral channel, at $4.92 \mu\text{m}$, with an excess of negative deviations from the mean spectrum. The associated pixels also show coherent spatial clustering. Further, this absorption feature correlates well with the anomalous bright feature known as Tui Regio (Fig. 26), previously reported and described (Barnes et al., 2006; McCord et al., 2006a) due to its anomalous brightness at $5 \mu\text{m}$ and its high $2.8/2.7\text{-}\mu\text{m}$. This $4.92\text{-}\mu\text{m}$ spectral feature at Tui Regio was independently noted by one of the authors (J. Barnes, personal communication), prior to its discovery using the techniques just described. Fig. 26c shows the scaled difference from the scene average spectrum, for the channels red = 4.94 , green = 4.92 , and blue = $4.90 \mu\text{m}$. This figure clearly shows a contiguous dark feature where Tui Regio appears in the false-color context image (Fig. 26a). Each of our search methods (simple deviation, scaled difference map, band-fitting) reveals this feature, although the one-channel deviation map shows the absorption most clearly, implying a narrow feature centered at $\sim 4.9 \mu\text{m}$.

Fig. 27 shows the spectrum of the negative and positive outliers found, as well as that of the contiguous Tui Regio feature. The average $4.92 \mu\text{m}$ band depth for the Tui Regio feature is just below the whole-scene noise level, defined as 1 SD from the scene average.

Note that the Tui Regio region has the highest $5\text{-}\mu\text{m}$ reflectance on all of Titan, and has 3–5 times the DN of any dark region (and therefore higher SNR) independent of the exposure duration. Since the whole-scene standard deviation is calculated including pixels of much lower albedo, the $4.9\text{-}\mu\text{m}$ feature is statistically significant when compared to the standard deviation among bright pixels only. Quantitatively, the “noise level” among all low-phase Titan pixels in the brightness-scaled cube CM1509136601 is $\sim 0.0020 I/F$ at $5.01 \mu\text{m}$, while the corresponding 1σ level for pixels with $5\text{-}\mu\text{m}$ I/F greater than the lowest-albedo Tui Regio pixels, is ~ 0.0011 , or 55% of the whole-scene SD (cf. Fig. 27). In comparison, the same number of low-albedo pixels has a SD of ~ 0.0027 , which gives approximately three times the statistical significance to the $4.9\text{-}\mu\text{m}$ Tui Regio feature compared to a hypothetical feature in the dark terrain.

One of the Tui Regio feature’s distinguishing characteristics is its anomalously high $2.8/2.7\text{-}\mu\text{m}$ band ratio. In the hope that it might allow identification of other similar features on Titan, we looked for a correlation between this ratio and the $4.92\text{-}\mu\text{m}$ band depth. The results (Fig. 28) show there is a linear correlation between the strength of the $4.92\text{-}\mu\text{m}$ absorption and the $2.8/2.7 \mu\text{m}$ band ratio, within the Tui Regio anomaly. The correlation coefficient $R = 0.74 \pm 0.06$ (95% confidence interval) for pixels showing the $4.9\text{-}\mu\text{m}$ band, with a corresponding probability of non-correlation $p \ll 10^{-9}$ ($N = 231$). Including all pixels in the scene yields $R = 0.70 \pm 0.04$, with $p \ll 10^{-9}$ ($N = 576$). This indicates that the material (or complex) responsible for the $4.92\text{-}\mu\text{m}$ feature also has the $2.8/2.7\text{-}\mu\text{m}$ spectral contrast (cf. Figs. 26b and 26c). Outside the Tui Regio anomaly, the correlation is much lower ($R = 0.34 \pm 0.08$), but still significant. Though other $5\text{-}\mu\text{m}$ bright anomalies have been observed by VIMS, their proximity to the limb and/or very lower SNR so far has precluded measurement of their $4.92\text{-}\mu\text{m}$ band depth.

7.2. Identification of the $4.92\text{-}\mu\text{m}$ feature material: CO_2 frost?

A search of spectral libraries does not suggest an obvious identification of this feature. Of the most likely materials to be associated with Titan’s surface, CO_2 frost has an absorption closest in wavelength to $4.92 \mu\text{m}$ (Fig. 29a). The CO_2 frost spectra presented here (and in Fig. 3b) are calculated using a two-stream Delta–Eddington plane albedo model described by Wiscombe and Warren (1980) and Hansen (1997) that we have used in other applications (e.g., Hansen, 2005; McCord et al., 2006a). We have resampled the CO_2 spectrum to VIMS spectral characteristics. Use of different grain sizes increases or decreases the strength of the absorption in CO_2 frost, with stronger absorption for larger grain sizes, but frosts with grain sizes larger than about $10 \mu\text{m}$ have the band saturated, so that measured I/F is zero. The wavelength position of the CO_2 absorption can be shifted, including to match the VIMS Titan

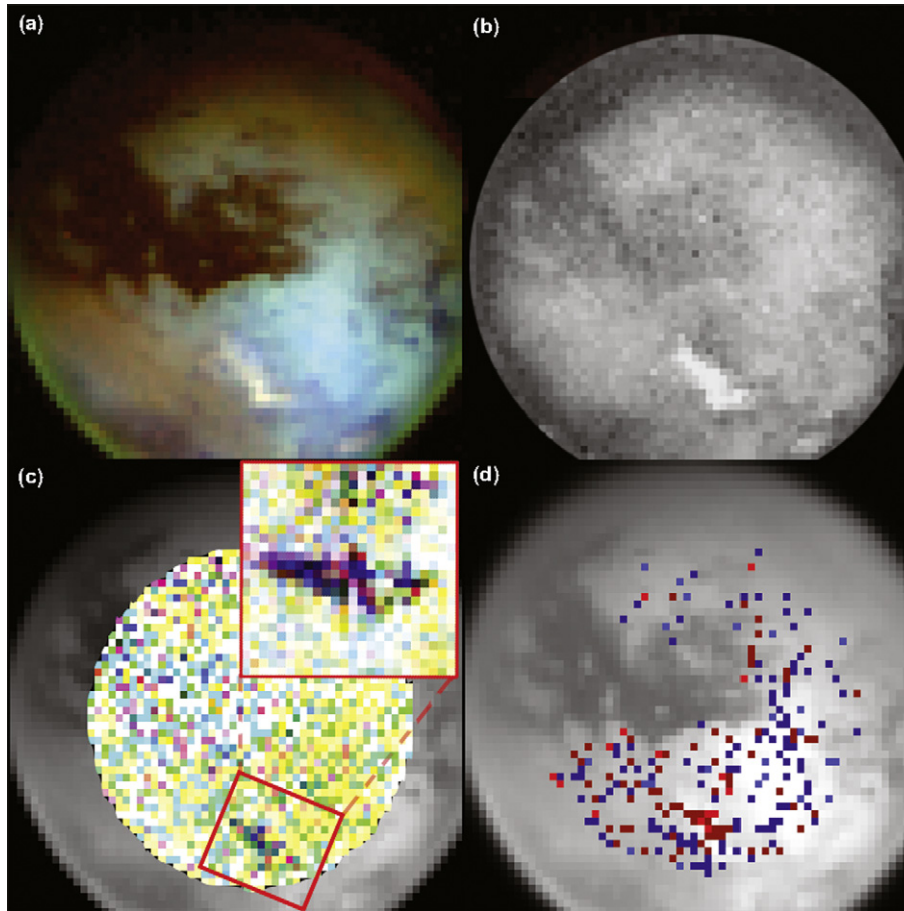


Fig. 26. The anti-saturnian hemisphere is shown (cube: V1509136601), with the Tui Regio bright feature at center-left; (a) is a false-color context image (red = 5.00, green = 2.03, blue = 1.28 μm). (b) shows the 2.8/2.7 μm ratio for the same dataset, where Tui Regio is visible as a bright anomaly. The central colored disk in (c) shows deviations from the whole-scene average spectrum, at the channels red = 4.94 μm , green = 4.92 μm , blue = 4.90 μm . The inset in this panel shows the same region, from another dataset (TI003). Tui Regio is clearly visible as a dark patch, indicating lower I/F in all three channels, particularly 4.92 μm . Panel (d) shows the negative (red) and positive (blue) 0.5- (dark) and 1-SD (bright) outliers, using a one-channel linear criterion.

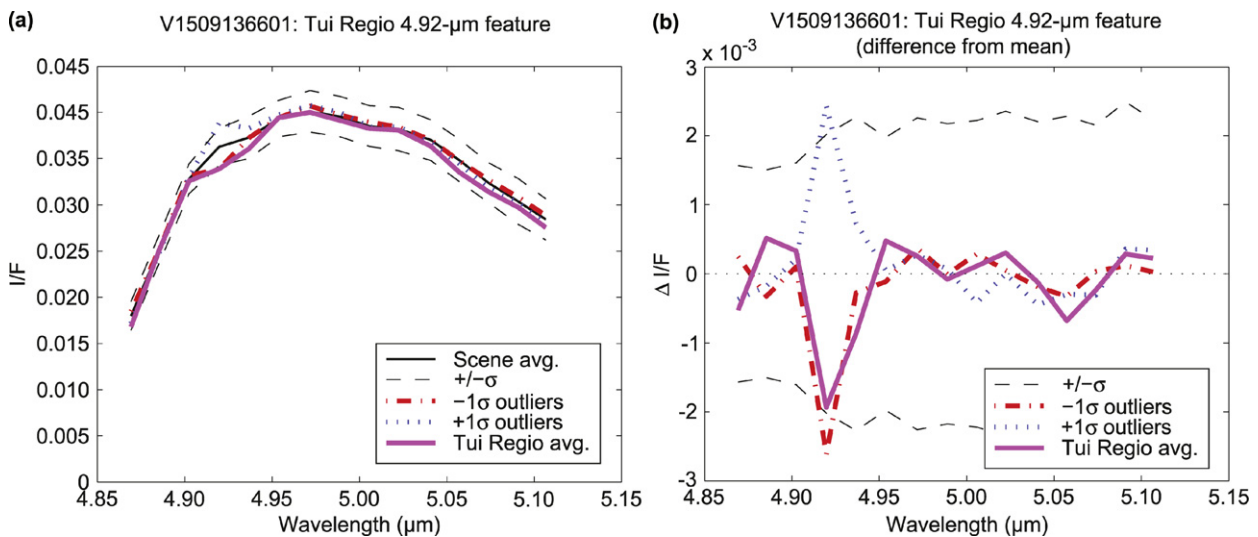


Fig. 27. (a) Average (scaled) 5- μm spectra are shown for the portion of Tui Regio appearing dark blue in the inset of Fig. 26c, as well as the one-channel outliers from 23 d, and two-channel outliers (not mapped). As usual, dashed black lines indicate one standard deviation from the scene average. (b) The same regions are plotted as in (a), this time as the difference from the scene average spectrum.

absorption, by bonding in different configurations (solid, liquid, gas, amorphous) and with different materials including as a re-

sult of radiation damage and associated induced chemistry (cf. discussions in McCord et al., 1998). It is beyond the scope of

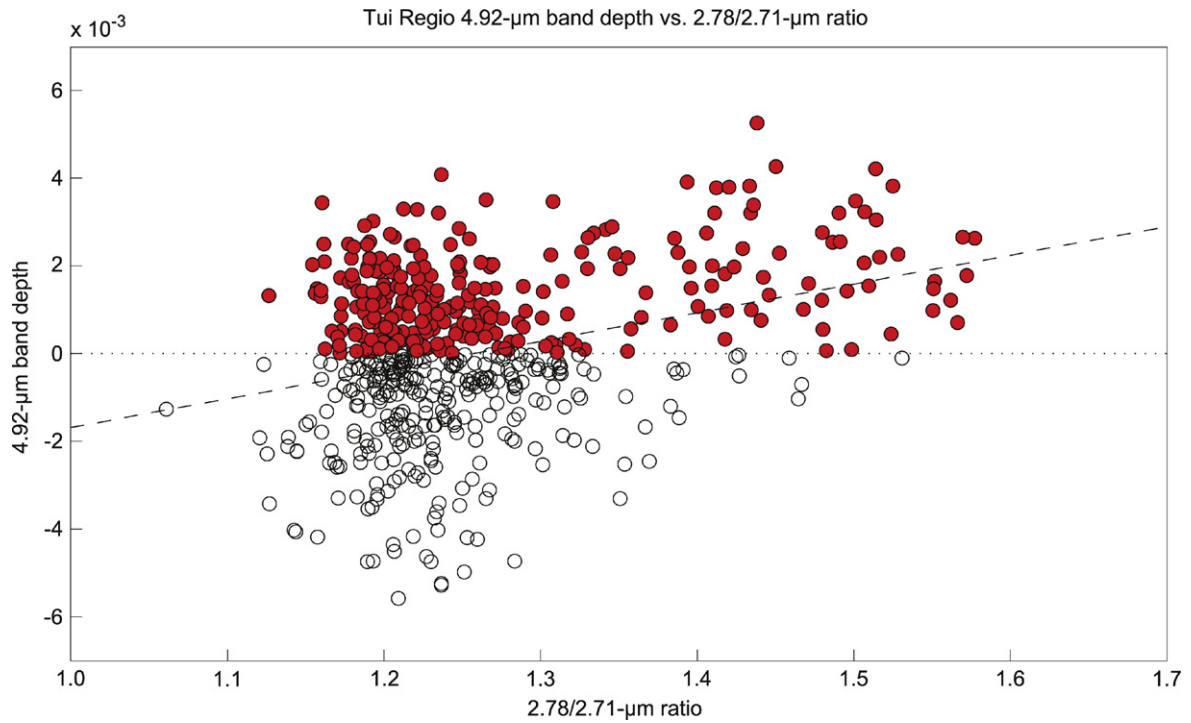


Fig. 28. Shown here is the correlation of 2.8/2.7-brightness ratio with the depth of 4.92- μm absorption for the Tui Regio feature. This indicates that the material responsible for the unusual brightness ratio within this methane window also exhibits the absorption.

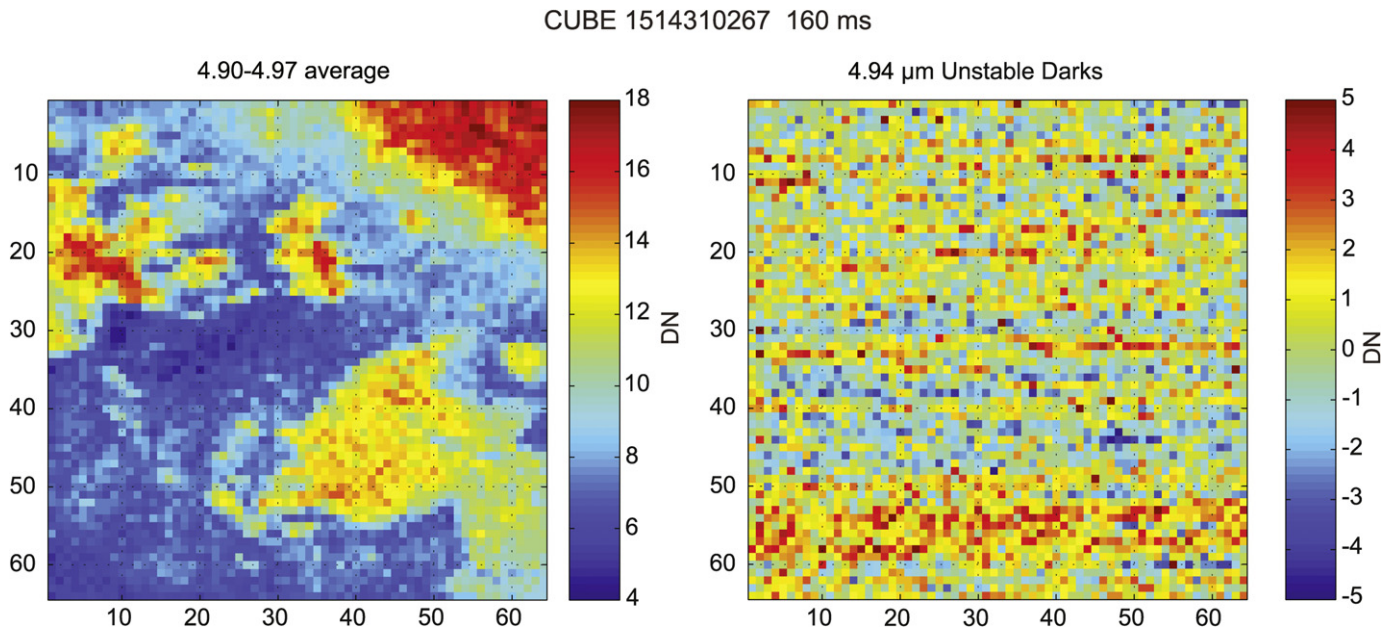


Fig. 29. An image of the region covered by VIMS IR data set 1514310267 (160 ms integration time) made by averaging all spectral channels between 4.90 and 4.97 μm is shown on the left. On the right is an image of the variations in the 4.94 channel data numbers due to variations in the dark signal.

this article to go further than the suggestion that CO_2 is a reasonable candidate for causing this absorption in the VIMS Titan spectrum.

While CO_2 is known to exhibit weak absorptions at ~ 1.97 , 2.01 and 2.07 μm , these would only reach detectable levels as the much stronger ~ 2.8 and 4.9 μm bands reached saturation. This would occur in the case of large grain sizes and/or abundances, and is not observed. Fig. 30 illustrates the effect

of convolving each of the 2.0- and the 4.9- μm CO_2 bands to the VIMS spectral response, using the laboratory spectra described previously (Hansen, 2005). Although their integrated absorbances are comparable, the 4.9- μm band is narrower and therefore more apparent in the VIMS data than the 2- μm bands. Unfortunately, the effective bandwidth of the convolved 2- μm absorption is comparable to the width of that methane window, and would therefore be manifested as a depression in the over-

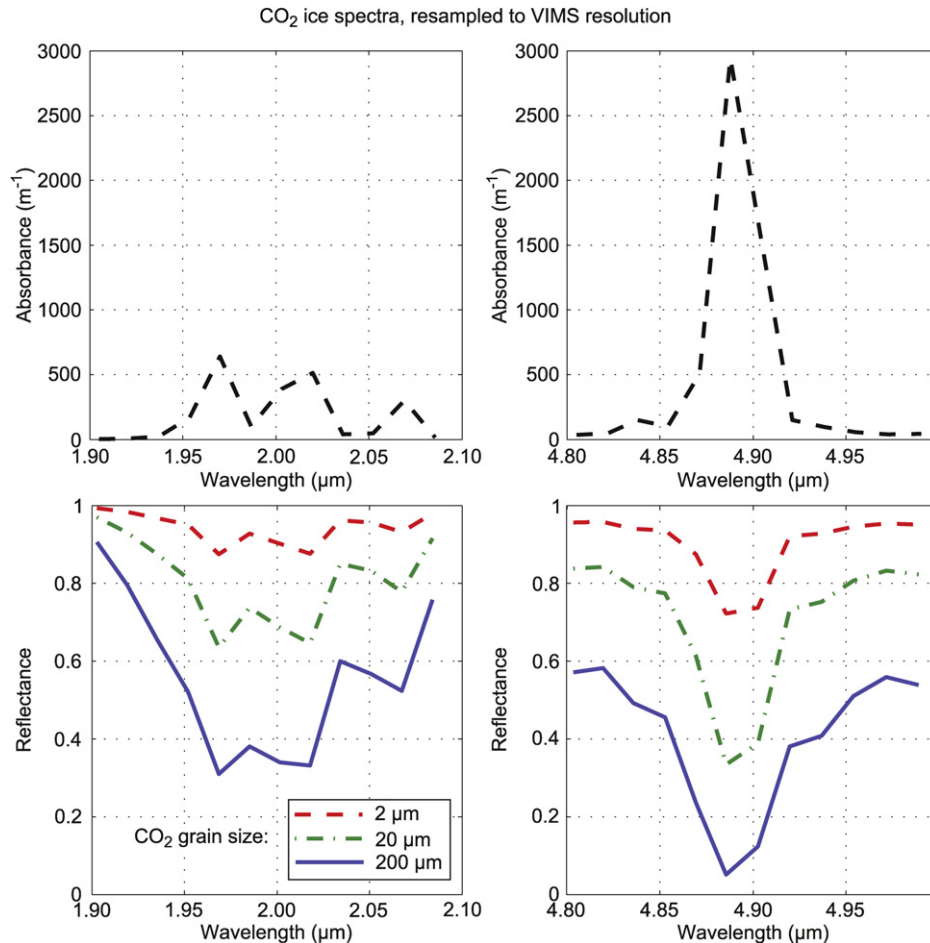


Fig. 30. Absorbance and reflectance for pure CO₂ ice, derived from optical constants measured in the laboratory by Hansen (2005).

all 2-μm reflectance, rather than as individual absorption lines. From the preceding argument, in a VIMS spectrum of pure CO₂ ice on the surface of Titan, we would expect the 4.9-μm band to appear stronger than the 2.0-μm bands.

Given their non-detection using the 2.0-μm CO₂ lines, Hartung et al. placed an upper limit on the spatial coverage of pure, monolithic CO₂ ice deposits, by assuming zero reflectance at 2.012-μm for such a deposit. Based on the ratio of the 1σ noise level to the surface signal (≈0.07 for bright regions), they calculated a maximum coverage by pure CO₂ of ~90 thousand km² per hemisphere for bright regions. By way of comparison, the surface area of Tui Regio (on the opposite hemisphere) is estimated to be ~200 thousand km². Even if Tui Regio were within the longitude range of the Hartung et al. study (which it is not), an areal mixture of up to 45% CO₂ would be allowed within their constraints. More realistically, intimate mixing with other surface materials should weaken, broaden, and shift the 2.012 and 2.070 μm lines, rendering them undetectable by VIMS and other instruments (Bernstein et al., 2005; see discussion below). In fact, we do not detect the 2.0-μm features, most likely for this reason, while the 4.9-μm feature is just above the noise level.

This tentative identification is consistent with the independent identification and mapping of a spectral unit with charac-

teristics similar to CO₂ frost in the spectral diversity and SMA analysis discussed earlier in Section 3. It is also consistent with CO₂ affecting the 3-μm spectral region of Titan from telescopic spectra (Coustenis et al., 2006). The evidence for CO₂ is further strengthened by noting that the spectrum of CO₂ frost can explain the contrast seen between the 2.8- and the 2.7-μm sub-windows, which is especially strong at Tui Regio (Fig. 24b and McCord et al., 2006a). In Fig. 27b we show a CO₂ frost reflectance spectrum overlaid on the 2.8-μm region Titan atmospheric transmission, using the same CO₂ grain size (2 μm radius) as for the Fig. 27a plot. The net result would be for the material to appear brighter in the longer-wavelength half of the overall window. Again, the contrast could be adjusted by changing or mixing the grain sizes and/or by mixing with spectrally neutral dark material. Smaller grain size CO₂ has greater 2.8/2.7 μm contrast and, as for the 4.92-μm feature, grain sizes over about 10 μm would result in saturation of the features and would no longer affect the contrast.

Fig. 31 (a, b) shows that the center wavelengths of the CO₂ absorption bands are shifted slightly from their nominal positions in the VIMS data. This shift can be explained by intimate mixing with other materials, which can alter bond vibrational frequencies. This phenomenon is observed in the laboratory,

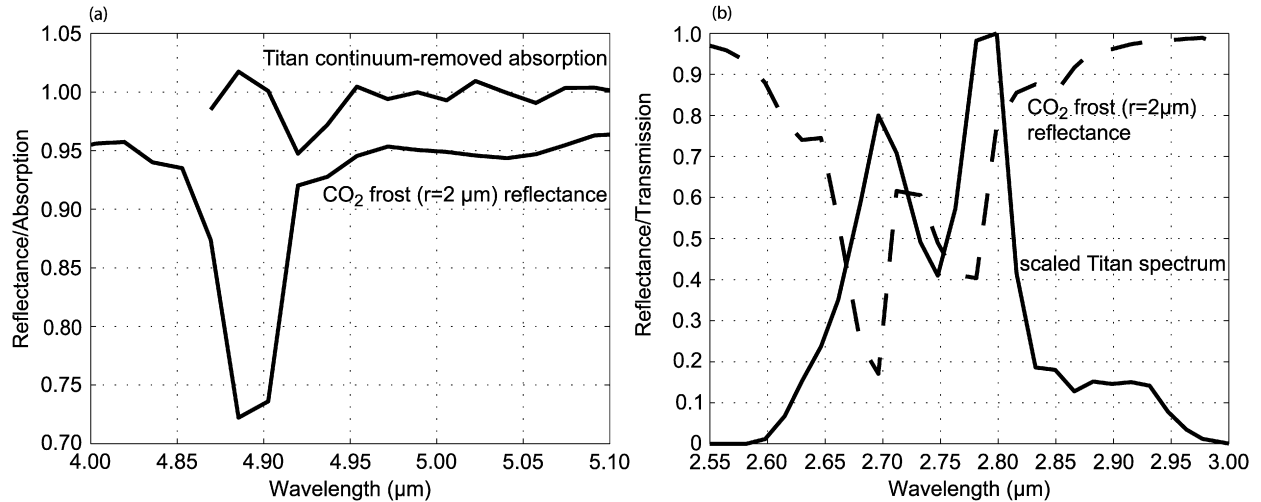


Fig. 31. A comparison of the laboratory spectrum of CO₂ frost and the VIMS spectrum of Tui Regio is shown for two different cases: (a) the Tui Regio region continuum-removed spectrum with the 4.92- μm absorption shown in Fig. 27 and (b) the reflectance in the 2.8- μm methane window. In Fig. 29a, the Titan absorption is close to but at a slightly longer wavelength than the CO₂ frost absorption. Error bars indicate the uncertainty in measured wavelength position (see text). In Fig. 29b, it is apparent that CO₂ frost would contribute more radiation to the longer-wavelength portion of the spectral window than to the shorter-wavelength portion. This is consistent with the contrast seen for the Tui Regio region and the material contributing the 4.92- μm absorption.

resulting in wavelength shifts of up to ~ 6 nm for H₂O/CO₂ mixtures (Bernstein et al., 2005). By convolving a wavelength-shifted CO₂ frost spectrum to VIMS spectral resolution, we estimate the uncertainty in the center wavelength of the observed VIMS ~ 4.9 - μm band to be 8.5 nm. Combined with an estimated uncertainty in the VIMS wavelength calibration of 6.9 nm, this gives a total RMS error of 11 nm. From this, we report the observed band at 4.920 ± 0.011 μm . Therefore, if this absorption is attributed to CO₂, a wavelength shift of ~ 13 nm long-ward from the laboratory-measured band center of 4.896 μm for pure CO₂ ice is required to match the VIMS band within our estimated uncertainty. This is within a factor of ~ 2 of the shift reported by Bernstein et al. (2005) for mixtures with H₂O, and therefore similar effects may be occurring on the surface of Titan.

8. Improvements in VIMS calibration

The data sets used here so far are the VIMS standard products, produced by the so-called “pipeline” processing using the VIMS standard calibrations. With tedious handwork, one can improve on this standard product. We have done this for a limited number of data sets, following methods developed mostly by G. Hansen first to treat Galileo Mission Near Infrared Mapping Spectrometer (NIMS) data and then adapted and applied to the VIMS data (e.g., Hansen et al., 2005, 2006), to better illustrate and compensate for some instrumental effects in the data.

8.1. The method

The standard pipeline VIMS IR channel data calibration subtracts backgrounds taken when the instrument focal plane chopper is closed, approximately once per line (Brown et al., 2004). If a radiation spike occurs during the background measurement,

its effect is propagated throughout the line by background subtraction; this is corrected by a routine in the pipeline processor that detects these spikes and removes their effect. A nominal despiking of the direct signal data is also performed.

The pipeline does not correct the residual thermal background of the instrument, which amounts to a 1–2 DN smaller background (larger signal) at each end of the spectrum (with more DN at longer integration times).

There are several channels, primarily coincident with channels that have excessive background current (showing as positive spikes in the background), that exhibit large variations (5–50 DN) in dark level. These variations occur for a few to several pixels at a time, and are not corrected by any pipeline processes because they affect only a small fraction of a line (Fig. 31). They can occur repetitively, covering a large (10–40%) portion of the image at these channels. They can be positive or negative, depending on the dark level adopted for the channel by the standard background processing. The unstable darks are localized in time, so they appear as artifacts localized along lines since the VIMS images are recorded as a raster scan. Because of their spatial distribution, the unstable darks can affect some averages more than others, and always affect low DN level averages more. More channels are affected by unstable darks and the magnitude of the dark variations is greater at larger integration times.

Residual small spikes not removed in the despiking can also affect averages, but are always positive, since the negative-going background spikes should be removed.

The residual thermal background can be corrected by measuring darks from deep space pixels, often on other observations close in time to the ones being processed. Since they vary with integration time, it is best to get an average from deep space observations with the same exposure, although the long-wavelength portion of thermal signal scales with integration time fairly accurately.

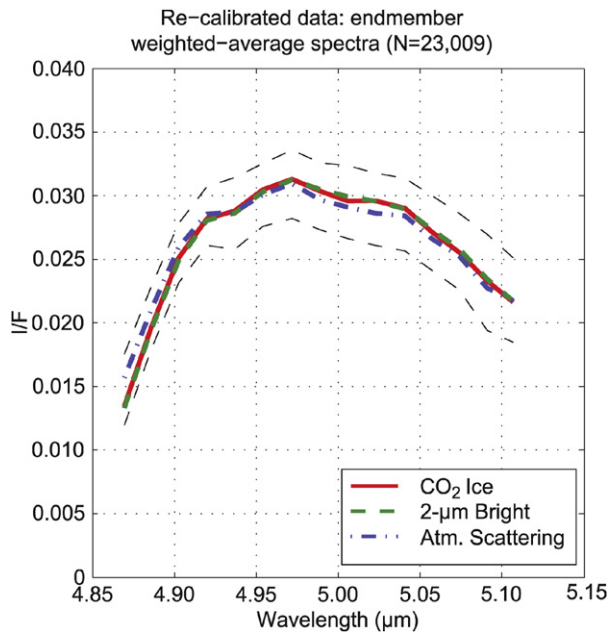


Fig. 32. The average spectrum in the 5- μ m window is shown for each of the major spectral units derived from the SMA and with one standard deviation from the mean shown in dashed lines. The data sets treated here were subject to the recalibration described in Section 8.1. This figure should be compared with Fig. 11, which is derived using the pipeline processed data.

The unstable darks are harder to determine accurately when objects are in the field of view. Subtracting a median of the data from the two channels before and two channels after the analyzed channel can produce an approximation of the darks, but this only works if the spectrum varies linearly in the region. Because of spectral curvature, subtracting a fraction near one times the local median can result in a better estimate, but the fractions are often dependent on the type of spectrum (ice, non-ice, Titan atmosphere, etc.). Where the DN's are small, the fraction is not as important (so using 1.0 for channels beyond 3 μ m is generally effective; see Fig. 31, which is generated this way).

When the signal is not too large, the difference image (rounded to the nearest multiple of 3 DN, to limit the propagation of noise) is subtracted from the data to correct the unstable darks. For the larger signal channels, an adjacent line averages within an image can be used to determine and correct unstable dark regions.

8.2. Application of recalibration method

Some of the VIMS datasets related to this study were recalibrated using the method described above. We show here the results of analyzing these recalibrated data to illustrate the affects of the instrumental effects as well as to give another measure of the confidence one can have in the analyses performed here and elsewhere.

We repeated our analysis of the spectral segments for the 5- μ m and the 2- μ m windows, using recalibrated data. The resulting 5- μ m weighted average spectra of the five spectral endmembers are plotted in Fig. 32, which is to be compared

with Fig. 9b, produced using the pipeline processed data. The recalibrated data average spectra are smoother in the long-wavelength region (with standard deviation >2 times smaller than in the pipeline calibration), but still show a pronounced dip at 4.94 μ m, which is the channel most troubled by unstable darks. Thus, it appears that the recalibration can help improve the data analysis and results but it is not perfect in correcting for the sometimes erratic nature of a few of the VIMS IR detector performance. The average spectra using the recalibrated data for the 2- μ m window are unchanged from Fig. 9a because the signal in the 2- μ m window is so much greater than in the 5- μ m window and the thermal and dark effects are relatively much smaller.

Acknowledgments

We thank Roger Clark for providing his laboratory spectrum of benzene plus carbon black and for detailed discussions of his spectral feature search algorithm. This article benefited from the comments by E. Lellouch and another anonymous reviewer. This research was supported by the NASA Cassini Project through the Jet Propulsion Laboratory.

References

- Ádámkóvics, M., de Pater, I., Hartung, M., Eisenhauer, F., Genzel, R., Griffith, C.A., 2006. Titan's bright spots: Multiband spectroscopic measurement of surface diversity and hazes. *J. Geophys. Res.* 111 (E7), doi:10.1029/2005JE002610. E07S06.
- Adams, J.B., Gillespie, A.R., 2006. *Remote Sensing of Landscapes with Spectral Images: A Physical Modeling Approach*. Cambridge Univ. Press, New York. 362 pp.
- Adams, J.B., McCord, T.B., 1971. Spectral reflectivity: Optical properties of mineral separates, glass and anorthositic fragments from Apollo mare samples. In: *Proceedings of the Apollo 12 Lunar Science Conference*, vol. 3. MIT Press, Cambridge, MA, pp. 2183–2195.
- Barnes, J.W., Brown, R.H., Turtle, E.P., McEwen, A.S., Lorenz, R.D., Janssen, M., Schaller, E.L., Brown, M.E., Buratti, B.J., Sotin, C., Griffith, C., Clark, R., Perry, J., Fussner, S., Barbara, J., West, R., Elachi, C., Bouchez, A.H., Roe, H.G., Baines, K.H., Bellucci, G., Bibring, J.-P., Capaccioni, F., Cerroni, P., Combes, M., Coradini, A., Cruikshank, D.P., Drossart, P., Formisano, V., Jaumann, R., Langevin, Y., Matson, D.L., McCord, T.B., Nicholson, P.D., Sicardy, B., 2005. A 5-micron-bright spot on Titan: Evidence for surface diversity. *Science* 310, 92–95.
- Barnes, J.W., Brown, R.H., Radebaugh, J., Buratti, B.J., Sotin, C., Le Mouélic, S., Rodriguez, S., Turtle, E.P., Perry, J., Clark, R., Baines, K.H., Nicholson, P.D., 2006. Cassini observations of flow-like features in western Tui Regio, Titan. *Geophys. Res. Lett.* 33, doi:10.1029/2006GL026843. L16204.
- Barnes, J.W., Brown, R., Soderblom, L., Buratti, B.J., Sotin, C., Rodriguez, S., Le Mouélic, S., Baines, K., Clark, R.N., Nicholson, P., 2007. Global-scale surface spectral variations on Titan seen from Cassini/VIMS. *Icarus* 186, 242–258.
- Bernard, J.-M., Quirico, E., Brissaud, O., Montagnac, G., Reynard, B., McMillan, P., Coll, P., Nguyen, M.-J., Raulin, F., Schmitt, B., 2006. Reflectance spectra and chemical structure of Titan's tholins: Application to the analysis of Cassini-Huygens observations. *Icarus* 186 (1), 301–307.
- Bernstein, M.P., Cruikshank, D.P., Sandford, S.A., 2005. Near-infrared laboratory spectra of solid H₂O/CO₂ and CH₃OH/CO₂ ice mixtures. *Icarus* 179 (2), 527–534.
- Boardman, J.W., Kruse, F.A., Green, R.O., 1995. Mapping target signatures via partial unmixing of AVIRIS data. In: *Summaries, Fifth JPL Airborne Earth Science Workshop*, vol. 1. JPL Publication 95-1, pp. 23–26.
- Bohren, C.F., Huffman, D.R., 1998. *Absorption and Scattering of Light by Small Particles*. Wiley, New York.

- Brown, R.H., Baines, K.H., Bellucci, G., Bibring, J.P., Buratti, B.J., Bussoletti, E., Capaccioni, F., Cerroni, P., Clark, R.N., Coradini, A., Cruikshank, D.P., Drossart, P., Formisano, V., Jaumann, R., Langevin, Y., Matson, D.L., McCord, T.B., Mennella, V., Miller, E., Nelson, R.M., Nicholson, P.D., Sicardy, B., Sotin, C., 2004. The Cassini Visual and Infrared Mapping Spectrometer investigation. *Space Sci. Rev.* 115, 111–168.
- Clark, R.N., Swayze, G.A., Livo, K.E., Kokaly, R.F., Sutley, S.J., Dalton, J.B., McDougal, R.R., Gent, C.A., 2003. Imaging spectroscopy: Earth and planetary remote sensing with the USGS Tetracorder and expert systems. *J. Geophys. Res.* 108, 5-1–5-43.
- Clark, R.N., Curchin, J.M., Brown, R.H., Waite, J.H., Cruikshank, D.P., Jaumann, R., Lunine, J., Hoefen, T.M., Cravens, T.E., Yelle, R.V., Vuitton, V., Baines, K.H., Buratti, B.J., Barnes, J., McCord, T.B., Nicholson, P.D., 2006a. Detection of widespread aromatic and aliphatic hydrocarbon deposits on Titan's surface observed by VIMS and excess benzene observed in Titan's thermosphere observed by INMS. *Bull. Am. Astron. Soc.* 38 (3), 574. Abstract 48-04.
- Clark, R.N., Curchin, J.M., Brown, R.H., Cruikshank, D.P., Jaumann, R., Lunine, J., Hoefen, T.M., Baines, K.H., Buratti, B.J., Barnes, J., Nicholson, P.D., 2006b. Detection of widespread aromatic and aliphatic hydrocarbon deposits on Titan's surface observed by VIMS. In: *Am. Geophys. Union Annual Fall Meeting Proceedings. Abstract P11A-03.*
- Clark, R.N., Curchin, J.M., Brown, R.H., Cruikshank, D.P., Jaumann, R., Lunine, J., Hoefen, T.H., Baines, K.H., Buratti, B., Barnes, J., Nicholson, P., Stephan, K., 2007. Detection of widespread aromatic and aliphatic hydrocarbon deposits on Titan. *Science*, submitted for publication.
- Combe, J.-Ph., Le Mouélic, S., Sotin, C., Gendrin, A., Le Deit, L., Mustard, J.F., Bibring, J.-P., Gondet, B., Langevin, Y., 2006. Omega Science Team analysis of OMEGA/Mars Express hyperspectral data using a linear unmixing model: Methods and preliminary results. *Lunar Planet. Sci.* 37. Abstract 2115.
- Coustenis, A., Negrão, A., Salama, A., Schulz, B., Lellouch, E., Rannou, P., Drossart, P., Encrenaz, T., Schmitt, B., Boudon, V., Nikitin, A., 2006. Titan's 3-micron spectral region from ISO high-resolution spectroscopy. *Icarus* 180, 176–185.
- Cruikshank, D.P., Allamandola, L.J., Hartmann, W.K., Tholen, D.J., Brown, R.H., Matthews, C.N., Bell, J.F., 1991. Solid C≡N bearing material on outer Solar System bodies. *Icarus* 94, 345–353.
- Flasar, F.M., and 44 colleagues, 2005. Titan's atmospheric temperatures, winds, and composition. *Science* 308, 975–978.
- Fulchignoni, M., Ferri, F., Colombatti, G., Zarnnecki, J.C., Harri, A.-M., Girard, R., Schwingenschuh, K., Hamelin, M., Lopez Moreno, J.J., Svedhem, H., and the HASI Team, 2005. First results on the characteristics of Titan's atmosphere by the Huygens Atmospheric Structure Instrument (9HASI) measurements. *European Geophysical Union Abstract A-05792, US9/PS1.5-1MO10-006.*
- Gaddis, L.R., Soderblom, L.A., Kieffer, H.H., Becker, K.J., Mullins, K.F., 1996. Decomposition of AVIRIS spectra: Extraction of surface reflectance, atmospheric and instrumental components. *IEEE Trans. Geosci. Remote Sensing* 34 (1), 163–178.
- Griffith, C.A., Owen, T., Geballe, T.R., Rayner, J., Rannou, P., 2003. Evidence for the exposure of water ice on Titan's surface. *Science* 300, 628–630.
- Grundy, W.M., Schmitt, B., 1998. The temperature-dependent near-infrared absorption spectrum of hexagonal H₂O ice. *J. Geophys. Res.* 103 (E11), 25809–25822.
- Grundy, W.M., Schmitt, B., Quirico, E., 2002. The temperature-dependent spectrum of methane ice I between 0.7 and 5 μm and opportunities for near-infrared remote thermometry. *Icarus* 155, 486–496.
- Hansen, G.B., 1997. Spectral absorption of solid CO₂ from the ultraviolet to the far-infrared. *Adv. Space Res.* 20, 1613–1616.
- Hansen, G.B., 2005. Ultraviolet to near-infrared absorption spectrum of carbon dioxide ice from 0.174 to 1.8 μm. *J. Geophys. Res.* 110, doi:10.1029/2005JE002531. E11003.
- Hansen, G.B., McCord, T.B., 2004. Amorphous and crystalline ice on the Galilean satellites: A balance between thermal and radiolytic processes. *J. Geophys. Res.* 109, doi:10.1029/2003JE002149. E012012.
- Hansen, G., McCord, T., Clark, R., Cruikshank, D., Brown, R., Baines, K., Bellucci, G., Buratti, B., Capaccioni, F., Cerroni, P., Combes, M., Coradini, A., Drossart, P., Formisano, V., Jaumann, R., Langevin, Y., Matson, D., Mennella, V., Nelson, R., Nicholson, P., Sicardy, B., Sotin, C., Soderblom, L., Hibbits, C., 2005. Ice grain size distribution: Differences between jovian and saturnian icy satellites from Galileo and Cassini measurements. *Eos (Fall Suppl.)* 86. Abstract #P11B-0124.
- Hansen, G.B., McCord, T.B., Hibbits, C.A., Kamp, L.W., 2006. Progress on the recalibration and rectification of Galileo NIMS spectral images of the Galilean satellites. *Eos (Jt. Assem. Suppl.)* 87 (36). Abstract P41B-05.
- Hapke, B., 1993. *Theory of Reflectance and Emittance Spectroscopy*. Cambridge Univ. Press, Cambridge, UK.
- Hartung, M., Herbst, T.M., Dumas, C., Coustenis, A., 2006. Limits to the abundance of surface CO₂ ice on Titan. *J. Geophys. Res.* 111 (E7). E07S09.
- Jaumann, R., Stephan, K., Brown, R.H., Buratti, B.J., Clark, R.N., McCord, T.B., Coradini, A., Capaccioni, F., Filacchione, G., Cerroni, P., Baines, K.H., Bellucci, G., Bibring, J.-P., Combes, M., Cruikshank, D.P., Drossart, P., Formisano, V., Langevin, Y., Matson, D.L., Nelson, R.M., Nicholson, P.D., Sicardy, B., Sotin, C., Soderblom, L.A., Griffith, C., Matz, K.-D., Roatsch, Th., Scholten, F., Porco, C.C., 2006. High-resolution Cassini-VIMS mosaics of Titan and the icy saturnian satellites. *Planet. Space Sci.* 54, 1146–1155.
- Lellouch, E., 2006. Titan's zoo of clouds. *Science* 311, 186–187.
- McCord, T.B., Hansen, G.B., Clark, R.N., Martin, P.D., Hibbits, C.A., Fanale, F.P., Granahan, J.C., Segura, M., Matson, D.L., Johnson, T.V., Carlson, R.W., Smythe, W.D., Danielson, G.E., and the NIMS Team, 1998. Non-water-ice constituents in the surface material of the icy Galilean satellites from the Galileo Near Infrared Mapping Spectrometer investigation. *J. Geophys. Res.* 103, 8603–8626.
- McCord, T.B., Coradini, A., Hibbits, C.A., Capaccioni, F., Hansen, G.B., Filacchione, G., Clark, R.N., Cerroni, P., Brown, R.H., Baines, K.H., Bellucci, G., Bibring, J.-P., Buratti, B.J., Bussoletti, E., Combes, M., Cruikshank, D.P., Drossart, P., Formisano, V., Jaumann, R., Langevin, Y., Matson, D.L., Nelson, R.M., Nicholson, P.D., Sicardy, B., Sotin, C., 2004. Cassini VIMS global observations of the Galilean satellites including the VIMS calibration procedure. *Icarus* 172, 104–126.
- McCord, T.B., Hansen, G.B., Buratti, B.J., Clark, R.N., Cruikshank, D.P., D'Aversa, E., Griffith, C.A., Baines, E.K.H., Brown, R.H., Dalle Ore, C.M., Filacchione, G., Formisano, V., Hibbits, C.A., Jaumann, R., Lunine, J.I., Nelson, R.M., Sotin, C., and the Cassini VIMS Team, 2006a. Composition of Titan's Surface from Cassini VIMS. *Planet. Space Sci.* 54, 1524–1539.
- McCord, T.B., Hayne, P., Combe, J.-P., Hansen, G.B., Baines, K.H., Brown, R.H., Buratti, B.J., Clark, R.N., Nicholson, P., 2006b. Titan surface composition analysis using VIMS. *Bull. Am. Astron. Soc.* 38 (3), 574–575. Abstract 48-05.
- McCord, T.B., Hayne, P., Combe, J.-P., Hansen, G.B., Barnes, J.W., Buratti, B., Haines, K.H., Brown, R.H., Nicholson, P., 2007. Titan: Surface composition from Cassini VIMS. In: *European Geosciences Union General Assembly. Geophys. Res. Abstract. ISSN: 1029-7006.*
- Mie, G., 1908. Beitrage zur Optik Truber Medien, speziell Kolloidaler Matalösungen. *Ann. Phys.* 25, 377–455.
- Nash, D.B., Conel, J.E., 1974. Spectral reflectance systematics for mixtures for powdered hypersthene, labradorite and ilmenite. *J. Geophys. Res.* 79, 1615–1621.
- Ramsey, M.S., Christensen, Ph., 1998. Mineral abundance determination: Quantitative deconvolution of thermal emission spectra. *J. Geophys. Res.* 103 (B1), 577–596.
- Rayleigh, L., 1971. On the light from the sky, its polarization and color. *Philos. Mag.* 41, 107–120, 274–279.
- Rodriguez, S., Le Mouélic, S., Sotin, C., Clénet, H., Clark, R.N., Buratti, B., Brown, R.H., McCord, T.B., Nicholson, P.D., Baines, K.H., and the VIMS Science Team, 2006. Cassini/VIMS hyperspectral observations of the Huygens landing site on Titan. *Planet. Space Sci.* 54 (15), 1510–1523.
- Roe, H.G., Brown, M.E., Schaller, E.L., Bouchez, A.H., Trujillo, C.A., 2005. Geographic control of Titan's mid-latitude clouds. *Science* 310 (5747).
- Singer, R.B., McCord, T.B., 1979. Large scale mixing of bright and dark surface materials and implications for analysis of spectral reflectance. *Proc. Lunar Sci. Conf.* 10, 1835–1848.
- Sobolev, V.V., 1975. *Light Scattering in Planetary Atmospheres*. Pergamon Press, Oxford.

- Soderblom, L.A., Brown, R.H., and the Cassini VIMS Investigation Team, 2005. Deconvolution of Cassini VIMS Titan cubes into atmospheric spectral scattering, surface topographic, and surface spectroscopic components. *Lunar Planet. Sci.* XXXVI. Abstract 1869.
- Soderblom, L.A., Kirk, R.L., Lunine, J.I., Anderson, J.A., Baines, K.H., Barnes, J.W., Barrett, J.M., Brown, R.H., Buratti, B.J., Clark, R.N., Cruikshank, D.P., Elachi, C., Janssen, M.A., Jaumann, R., Karkoschka, E., Le Mouélic, S., Lopes, R.M., Lorenz, R.D., McCord, T.B., Nicholson, P.D., Radebaugh, J., Rizk, B., Sotin, C., Stofan, E.R., Sucharski, T.L., Tomasko, M.G., Wall, S.D., 2007. Correlations between Cassini VIMS spectra and RADAR SAR images: Implications for Titan's surface composition and the character of the Huygens Probe Landing Site. *Planet. Space Sci.*, submitted for publication.
- Stofan, E.R., and 35 colleagues, 2006. Mapping of Titan: Results from the first Titan radar passes. *Icarus* 185 (2), 443–456.
- Swayze, G.A., Clark, R.N., Goetz, A.F.H., Chrien, T.G., Gorelick, N.S., 2003. Effects of spectrometer band pass, sampling, and signal-to-noise ratio on spectral identification using the Tetracorder algorithm. *J. Geophys. Res.* 108, 9-1–9-30.
- Tomasko, M.G., Archinal, B., Becker, T., Bézard, B., Bushroe, M., Combes, M., Cook, D., Coustenis, A., de Bergh, C., Dafoe, L.E., Doose, L., Douté, S., Eibl, A., Engel, S., Gliem, F., Grieger, B., Holso, K., Howington-Kraus, E., Karkoschka, E., Keller, H.U., Kirk, R., Kramm, R., Küppers, M., Lanagan, P., Lellouch, E., Lemmon, M., Lunine, J., McFarlane, E., Moores, J., Prout, G.M., Rizk, B., Rosiek, M., Rueffer, P., Schröder, S.E., Schmitt, B., See, C., Smith, P., Soderblom, L., Thomas, N., West, R., 2005. Rain, winds and haze during the Huygens probe's descent to Titan's surface. *Nature* 438 (7069), 765–778.
- van de Hulst, H.C., 1981. *Light Scattering by Small Particles*. Dover, New York.
- Wiscombe, W.J., Warren, S.G., 1980. A model for the spectral albedo of snow. I. Pure snow. *J. Atmos. Sci.* 37, 2712–2733.